Corso di Laurea Magistrale

in Ingegneria Chimica e dei Processi Sostenibili

Tesi di Laurea Magistrale

Enhancing Pt/CeO_2 Catalysts for VOC Oxidation by Modulating Ceria Surface Area and Platinum Dispersion

Relatori

Samir Bensaid

Nunzio Russo

Enrico Sartoretti

Candidato

Pietro Gaudio

S322364

Marzo 2026

Summary

1.Introduction

The term 'Volatile organic compounds' (VOCs) covers a vast class of carbon based substances with peculiar properties, such as the high volatility and the resistance to degradation. In scientific literature many definitions are present. For instance, in the directive 2004/42/CE the European Union stated that the term 'VOC' refers to any organic compound having an initial boiling point equal to or less than 250°C at the standard pressure of 101,3 kPa. In 1989 The World Health Organization proposed a classification of VOCs based on their boiling point, dividing these compounds into three categories: Very Volatile Organic Compounds, VOCs and Semi Volatile Organic Compounds, as shown in Table 1.1

Tabella 1.1

Category	Boiling point range, °C
Very Volatile Organic Compounds - VVOC	< 0 to 50-100
Volatile Organic Compound - VOC	50-100 to 240-260
Semi Volatile Organic Compound - SVOC	240-260 to 380-400

Many classes of substances are included in these general definitions, as alcohols, hydrocarbons, halides, organic acids, ketones, esters and more. In fact, more of 500 compounds belong to VOC category. However, the composition of a particular VOC is function of its source, that can be related to biobased or anthropic phenomena (Pandey & Yadav, 2018).

1.1 Biogenic Sources

Biogenic sources mostly include:

- Emissions from plants and vegetation
- Volcanic phenomena
- Combustions of biomass and organic material

Emissions from vegetation are strictly linked to atmospheric chemistry. The main types of compounds emitted are isoprene and monoterpenes. These compounds play a key role in tropospheric processes, particularly in the formation of atmospheric haze and ozone. In fact, due to their high reactivity, these substances have a strong influence on regional air quality, oxidation capacity of the troposphere and ozone structure. Emissions originate from foliage, with strong dependence on plant species, vegetation type, and environmental conditions [2]

Volcanic Phenomena can dramatically change the ordinary atmospheric composition, causing wide emission of gases with both magmatic and hydrothermal components. In these mixtures, the VOC fraction is dominated by Alkanes, Alkenes and Aromatic hydrocarbons. In addition to these major groups, the emissions contain minor but chemically significant

amounts of Oxygen substituted compounds (e.g. alcohols, esters, aldehydes) and Halogenated species, particularly Cl- and F-substituted hydrocarbons [3].

Vegetation fires constitute a major source of biogenic volatile organic compounds (BVOCs), releasing copious quantities of highly reactive organic species into the atmosphere. The BVOC emissions associated with fires are dominated by isoprenoid compounds, primarily isoprene, monoterpenes and sesquiterpenes, which contain one or more carbon–carbon double bonds and therefore exhibit high chemical reactivity. These compounds are emitted not only during active combustion but also during earlier and peripheral stages of fire development, such as vegetation drying and thermal stress at the fire front, when unburned plants respond to heat exposure by releasing substantial amounts of BVOCs. As a result, forest fires can profoundly modify both the magnitude and chemical composition of BVOC emissions relative to undisturbed vegetation [4]

For the sake of completeness, other sources of BVOCs are:

- Animals, since VOCs are fundamental molecules for self-defense, metabolism and they are emitted even during feeding operation (Yuan et al., 2017).
- Ocean, due to reactions occurring at Air-Water interface [6]

Natural emissions of VOCs are predominantly responsible for air composition in outdoor environments. Outdoor environment refers to the physical space outside built or enclosed structures, encompassing the ambient atmosphere and natural or seminatural surroundings in which human activities, ecosystems, and climatic processes interact. It includes open air settings such as urban areas, rural landscapes, and natural environments, where environmental factors play a critical role in influencing human health and ecological balance. According to the World Health Organization (2018), the outdoor environment is especially relevant for the assessment of ambient air pollution, as it represents the primary medium through which pollutants are transported, transformed, and ultimately inhaled by populations.

BVOCs represent the 90% of the total VOCs emission, since Biogenic sources emit around 1000 TgC/yr (teragrams of Carbon per year) [2].

1.2 Antropogenic emissions

Volatile organic compounds (VOCs) generated by anthropogenic activities arise from a wide range of domestic, commercial, agricultural, and industrial processes and represent a major class of air pollutants at both local and global scales. [1]

These compounds account for approximately 10% of total VOC emissions. However, in comparison with naturally emitted organic substances, anthropogenic VOCs are significantly more amenable to regulation and control through targeted technological and policy interventions.

Anthropic sources of VOCs can be broadly classified into two main categories:

- stationary sources
- mobile sources

Stationary sources are defined as fixed, immobile installations, such as industrial facilities, oil refineries, power generation plants, and large-scale boilers, that emit pollutants directly into the atmosphere from specific, localized points. These sources typically operate continuously or for extended periods and are often characterized by identifiable emission outlets, such as smokestacks or vents. In contrast, mobile sources include vehicles and other modes of transportation, such as cars, trucks, buses, ships, aircraft, and rail systems, which generate and release pollutants while in operation. Unlike stationary sources, mobile sources are dispersed across wide geographic areas and produce emissions intermittently as they move, making their monitoring and regulation more complex [7]

Anthropic sources influence indoor and outdoor quality of air. In terms of outdoor environments, a substantial proportion of atmospheric VOCs originates from transportation related activities. Emissions from motor vehicles vary depending on several factors, including vehicle type, meteorological conditions, ambient temperature, and temporal variables such as the time of day, week, and year. Additional anthropogenic VOCs, particularly Benzene, Toluene, Ethylbenzene, xylene (BTEX compounds) and chlorinated aromatic hydrocarbons, are released from stationary sources through various industrial and energy related processes. These include crude oil refining and accidental releases during tanker operations; the combustion of fossil fuels in power generation and heating plants; the use of solvents such as carbon tetrachloride, dichloromethane, chloroform, and BTEX compounds; and the manufacture of synthetic materials, including synthetic fibers (e.g., nylon), resins, paints, solvents, dyes, and pesticides [8].

The diagram showed in Figure 1.1 underlines how in Europe the main source of VOCs are the industrial process, followed by founts related to ordinary urban activities, agriculture and transport sector.

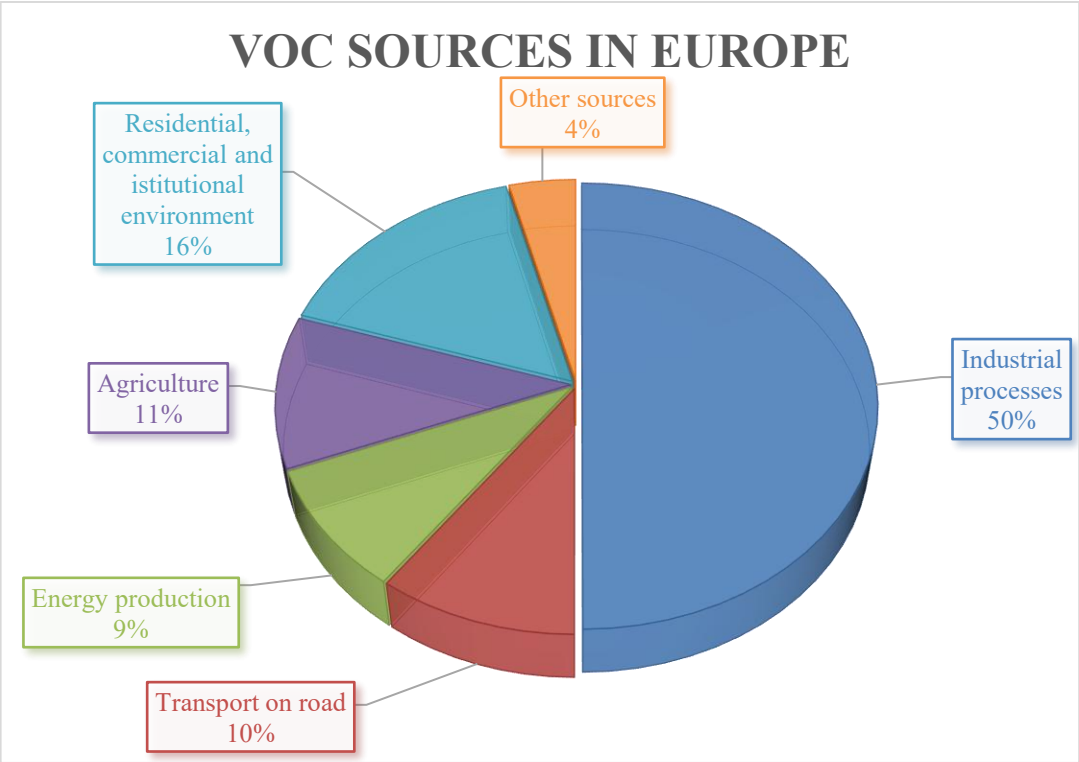

Figure 1.1. Sources of VOC emission in the EU area. Source: From “Air quality in Europe – 2017 report” EEA Report No 13/2017 with modifications.

On the other hand, indoor environments are confined ones and, according to the Italian Ministry of Health (2023), they include:

- Residential buildings
- Public and private offices
- Community facilities (e.g., hospitals, schools, administrative offices, military barracks, hotels, banks)
- Spaces dedicated to recreational and social activities (e.g., cinemas, bars, restaurants, retail stores, sports facilities)
- Public and private means of transportation (e.g., cars, trains, airplanes, ships)
- residential buildings
- public and private offices

Although industrial environments are excluded from the definition of indoor or confined spaces, as indoor air in such settings is intricately linked to the specific industrial processes, in this paragraph even the presence of VOC in these particular contexts will be discussed.

Indoor environments constitute the primary settings in which human exposure to VOCs occurs, as individuals typically spend approximately 90% of their time indoors. For this reason, indoor spaces represent a critical context for the assessment of air quality, particularly with respect to the presence, composition, and concentration of VOCs [9].

Consequently, the systematic analysis of indoor VOCs levels, their sources, their temporal variability, and even their mechanism of transport is of fundamental importance for accurately characterizing human exposure, understanding indoor air chemistry, and supporting the development of effective ventilation strategies and exposure mitigation measures, as it will be analyzed in the next paragraphs.

Indoor air primarily originates from outdoor (ambient) air and enters enclosed spaces through ventilation processes, which may be natural and/or mechanical. Focusing firstly on domestic environments, VOCs are among the most common indoor air pollutants and are frequently detected at concentrations higher indoors than outdoors. They may be emitted by building materials and furnishings such as carpets, paints, wallpapers and polyvinyl chloride (PVC), infiltrate from outdoor air, or be generated by indoor human activities including cooking and tobacco smoking [10].

VOC transport is also influenced by diffusion across walls and other structural elements, enabling compounds to move into and out of indoor spaces, while indoor materials may act as buffers by reducing peak airborne concentrations but prolonging the persistence of VOCs in the indoor environment. Experimental investigations of VOC diffusion and sorption in indoor materials have shown that, for certain materials, effective diffusion coefficients are only one order of magnitude lower than those measured in air, highlighting the relevance of material mediated transport processes [11]

Chemical analyses conducted in residential environments have identified indoor pollution dominated by compounds such as ethanol, acetone, acetic acid and 1-methoxy-2-propanol, which significantly alter the VOC distribution typically expected for standard dwellings and are widely used as solvents in industrial activities. Figure 1.2 unveils the mean distribution of VOCs in the air of a flat in Barcelona in 2006:

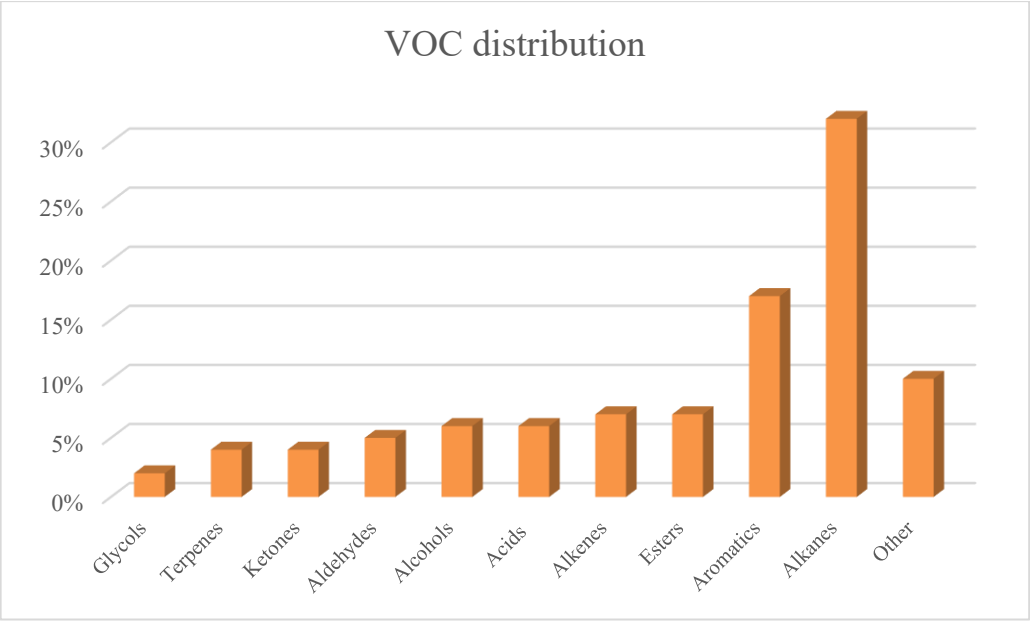

Figure 1.2. VOC family distribution in dwelling modified from (Gallego et al., 2009).

Comparisons with reference values from dwellings unaffected by industrial sources indicate that, in such cases, the primary origin of indoor VOC contamination is external [12]

Research on indoor airborne chemical sources has traditionally focused on outdoor air infiltration, building materials, furnishings and occupant related activities such as smoking, cooking and cleaning, while comparatively limited attention has been paid to direct occupant emissions, despite their clear contribution to indoor VOC levels and indoor chemistry. The most abundant compounds detected included VOCs associated with personal care products, as well as metabolic emissions such as isoprene, methanol, acetone and acetic acid, with additional contributions arising from ozone driven oxidation of human skin oils, producing secondary compounds such as 4-oxopentanal and 6-methyl-5-hepten-2-one. On a mass basis, human-emitted VOCs constituted the dominant source during occupied periods in a well-ventilated classroom, accounting for approximately 57% of total VOC emissions, followed by ventilation supply air at 35% and indoor non occupant sources at 8%, with a total occupant associated VOC emission factor estimated at 6.3 mg h^{-1} per person [13]

Moving to the industrial environment, as previously noted, it is difficult to generalize the sources of VOC emissions, as these are strongly dependent on the specific activities carried out within each workplace. Industrial processes vary widely in terms of raw materials, technologies, and operational conditions, all of which influence both the nature and magnitude of VOC emissions. Consequently, a sector specific approach is required to properly characterize VOC sources and exposure scenarios.

The following section focuses in particular on the occurrence of VOCs within chemical industry settings, encompassing a broad range of activities from petrochemical production to the printing industry. These sectors are known for their intensive use of organic solvents, resins, inks, and chemical intermediates, which represent significant sources of VOC emissions during manufacturing, handling, and storage processes. In addition, attention is given to office environments associated with industrial facilities, where VOCs may originate from building materials, office equipment, cleaning products, and ventilation systems [14]

Other notable examples of industrial processes that contribute to the emission VOCs include chemical and pharmaceutical manufacturing facilities, which often release these compounds during the synthesis and formulation of products. The automobile industry, particularly in the production and painting of vehicles, generates substantial VOC emissions as well. In the food processing sector, volatile organic substances are emitted as a byproduct of processes like sterilization, extraction, and packaging. Additionally, textile manufacturing plants, with their use of dyes, solvents, and other chemicals, are another significant source. Finally, electronic component production facilities, which involve the use of solvents and other volatile substances in the assembly and finishing stages, also contribute to the release of these compounds into the atmosphere. [15]

In petroleum refining and petrochemical industries, process emissions arise from:

- core industrial operations, such as separation, conversion, and treatment processes, including cracking, reforming, and isomerization. The extensive processing and transformation of hydrocarbons in these activities result in VOC emissions, escaping primarily through safety valve discharges, process vents, and sampling points. The compounds most commonly associated with these emissions include benzene, toluene, ethylbenzene, and xylenes (BTEX), which are intrinsic constituents or byproducts of petroleum-derived streams.
- Fugitive emissions, namely unintended releases of VOCs resulting from equipment leaks rather than controlled discharge points. In petrochemical installations, these emissions arise from compressors, pumps, valves and piping flanges, leading to both continuous low-level leaks and episodic releases. The compounds involved largely mirror those handled within the process streams, particularly benzene and other light aromatic hydrocarbons.
- Storage and handling operations, mainly attributed to evaporative losses, including boiling losses and breathing losses caused by temperature-induced expansion and contraction of vapor spaces within storage tanks.
- combustion emission, primarily originate from stationary combustion sources, such as furnaces, heaters, and steam boilers, as well as from flares used intermittently during operational upsets to safely dispose of excess hydrocarbons. The emission profile depends on the type of fuel and combustion conditions but typically includes nitrogen oxides (NO_x), sulfur dioxide (SO_2), carbon monoxide, and residual VOCs. Combustion-related VOC emissions are generally lower than process-related ones.

Additional auxiliary sources include cooling towers, wastewater treatment units, boilers, and sulfur recovery units. [16], [17]

Collectively, these emission sources constitute significant vectors for the elevation of VOC concentrations within two distinct environments. Firstly, they exert a profound influence on occupational exposure levels within enclosed petrochemical industrial settings. Secondly, via atmospheric transport and dispersion, these emissions contribute substantially to the anthropogenic background levels in residential vicinities situated on the periphery of the refinery [18]

Focusing on other working environments, it is meaningful cite a study conducted by Saraga et al., aimed to identify VOCs and other pollutants sources and concentrations in two indoor environments of different use: a printery industry and an office,. The monitored pollutants included particulate matter, inorganic pollutants, and organic compounds (BTEX and

formaldehyde).Variations in indoor activities, equipment usage, occupancy levels, ventilation patterns, and outdoor background conditions significantly influenced pollutant concentrations across sites.

The printery industry exhibited the highest average concentrations of benzene (69.4 μg m^{-3}), toluene (147 μg m^{-3}). Benzene and toluene peaks were particularly pronounced in the presser section, reflecting emissions from printing inks, solvents, and mechanical processes. In contrast, office environments showed the highest concentrations of m,p-xylene and o-xylene, especially in non-smoking offices, with values of 241 μg m^{-3} and 174 μg m^{-3}, respectively. These elevated levels are likely attributable to photocopiers, printers, and adhesive materials used during interior renovation activities, such as tile installation [19].

To conclude the review of anthropogenic VOCs emissions, Table 1.2 provides a comprehensive overview of specific compounds and their associated origins in enclosed settings:

VOCs	**Source**
ethanol, acetone, methanol	perfumes, cleaning supplies, products for hair and nails
ethylene, isobutylene	rubber
benzene, toluene and other aromatics	Scented products, cigarettes and tobacco smoke, insulation material,
formaldehyde	furniture, carpets
cyclohexane, n-butane, n-hexane	leather, furniture, cosmetic products
difluoromethane, tricloroethane	refrigeration cycle
acetone and other ketones	PVC cement and adhesives
ethers	medical solvents

Table 1.2. VOCs type and sources in indoor environments modified from *[14]*

1.3 Environmental Impact of VOCs

The aim of this subchapter is to examine the environmental impacts of VOCs, especially the ones emitted in indoor and outdoor context. This topic that has been extensively investigated in the scientific literature due to the significant role in atmospheric processes of this substances and their potential adverse effects on ecosystems and human health. In this sense, it is fundamental to analyze the mechanism of transport of VOCs.

The physicochemical behavior of these compounds is dictated largely by their volatility. High volatility facilitates the release of compounds from solids and liquids into the gaseous phase. Consequently, Very Volatile Organic Compounds (VVOCs) and Hazardous Air Pollutants (HAPs) are predominantly found as gases in the atmosphere rather than on surfaces. Conversely, less volatile compounds partition significantly into solid or liquid

phases, adhering to dust, construction materials, or vegetation surfaces. Once released, VOCs undergo complex transport and transformation processes. They may partition between gas and particle phases, influencing their atmospheric lifetime and deposition. Meteorological conditions allow for long-range transport across continents, often bound to fine particulate matter. In cold or humid climates, VOCs may adsorb onto surfaces, only to re-volatilize when temperatures rise. [20]

The ecological footprint of VOCs is profound, affecting atmospheric chemistry, climate stability, and biological physiology. The environmental impacts can be categorized into four primary mechanisms:

- Stratospheric ozone depletion: certain classes of VOCs, particularly halogenated hydrocarbons such as chlorinated compounds, are characterized by high chemical stability and low reactivity in the troposphere. Due to their resistance to degradation and removal processes, these substances, classified as ozone-depleting substances (ODS), can persist long enough to be transported into the stratosphere. Under stratospheric conditions, exposure to high energy ultraviolet radiation induces their photolytic decomposition, releasing halogen radicals that participate in catalytic cycles responsible for the destruction of ozone molecules. The resulting depletion of the stratospheric ozone layer enhances the transmission of biologically harmful ultraviolet (UV-B) radiation to the Earth's surface, leading to adverse effects on human health, terrestrial and aquatic ecosystems, and plant physiology. [21]
- Photochemical Smog and Tropospheric Ozone Formation : in the troposphere, volatile organic compounds (VOCs) play a fundamental role as primary precursors in the generation of secondary atmospheric pollutants. Through complex photochemical reaction pathways initiated by solar radiation and mediated by nitrogen oxides (NO_x) and hydroxyl radicals (OH•), VOCs significantly enhance the production of ground-level ozone and secondary oxidants such as peroxyacetyl nitrate (PAN). These species constitute key components of photochemical smog and are responsible for adverse effects on air quality and human health. The relative ability of individual VOCs to promote ozone formation is quantified by their Photochemical Ozone Creation Potential (POCP). Unsaturated hydrocarbons, including propene, as well as aromatic compounds, exhibit particularly high POCP values and are also strongly associated with the formation of secondary organic aerosols (SOAs). [22]
- Greenhouse effect and climate change: Volatile organic compounds (VOCs) contribute to climate change through both direct and indirect mechanisms. Directly, certain VOCs participate in radiative forcing by absorbing and re-emitting infrared radiation, thereby influencing the Earth's energy balance. Indirectly, VOCs play a significant role as chemical precursors in the formation of tropospheric ozone (O_3) and secondary organic aerosols (SOAs), both of which act as effective greenhouse agents and modulate atmospheric radiative properties. Among VOCs, chlorinated organic compounds are of particular concern due to their high persistence and strong climatic impact; when assessed over a 100-year time horizon, their Global Warming Potential (GWP) can range from approximately 10 to 1800 times that of carbon dioxide (CO_2), underscoring their disproportionate contribution to long-term global warming. [23], [24]
- Ecological toxicity and biotic stress: Ground-level ozone and other reactive gaseous byproducts exert significant stress on biological systems by interfering with fundamental physiological processes in vegetation, including chlorophyll synthesis, photosynthetic carbon assimilation, and respiratory metabolism. Prolonged exposure to

elevated ozone concentrations can impair plant growth, reduce biomass accumulation, and decrease ecosystem productivity. In addition, several volatile organic compounds (VOCs), such as benzene and formaldehyde, are well-documented for their carcinogenic, mutagenic, and endocrine-disrupting properties. Chronic environmental exposure to these compounds has been associated with immunosuppression in aquatic organisms, disruptions in reproductive and developmental processes, and alterations in microbial community composition and functionality, with potential cascading effects on ecosystem stability and biogeochemical cycles. [20]

Moreover, there is a critical feedback loop between climate change and VOC emissions. Temperature is a primary driver of VOC release from both biological and non-biological sources. Studies indicate that ongoing global warming is accelerating VOC emissions at twice the rate of rising temperatures. This is particularly evident in arctic ecosystems, where emissions are expected to rise substantially. Elevated temperatures and soil moisture variations influence plant communities and biomass, leading to alterations in the chemical evolutionary trajectory of VOC emissions. In turn, the oxidation of these increased VOC loads, often exacerbated by higher concentrations of CO2 and carbon monoxide (CO), leads to further aerosol production, creating a cycle that potentially accelerates climate warming. [25]

In order to complete the analysis of the environmental impacts associated with volatile organic compounds (VOCs), it is essential to examine the legislative framework governing their emission and exposure limits. Regulatory measures constitute a central component of risk management, as they establish binding thresholds, monitoring requirements, and compliance mechanisms aimed at protecting both public health and the environment. In the Italian context, emissions of VOCs are regulated under Legislative Decree No. 152/2006 (D.Lgs. 152/06), which represents the primary national environmental code. This decree incorporates specific provisions concerning volatile organic compounds, particularly in relation to industrial activities involving the use of organic solvents. The legislation establishes emission limit values for total VOC releases, defines technical criteria for monitoring and measurement, and specifies methodologies for verifying compliance with prescribed thresholds. Furthermore, D.Lgs. 152/06 outlines the procedures for the preparation and implementation of solvent management plans, which are required for installations exceeding defined consumption thresholds. These plans aim to quantify solvent inputs and outputs, identify emission sources, and promote the adoption of mitigation strategies. The regulatory framework also encourages the substitution of high solvent content materials with low or zero solvent alternatives and the optimization of operational processes to minimize emissions at source. [26]

1.4 Health impact of VOCs

Health effects of VOCs have strong relevance in indoor settings, since individuals spend most of their lives in confined spaces, as already mentioned. In indoor environments, measured VOC concentrations obtained from fixed location monitors do not necessarily represent an individual's true exposure. Many important emission sources are closely tied to personal behaviors, including smoking, cooking, cleaning, and the use of personal care products, so that inhalation exposure can be substantially higher than what is suggested by room-average indoor air measurements. This phenomenon, often termed the 'personal cloud effect', has been reported to yield exposure levels approximately two to four times higher than stationary monitoring would indicate.[27]

The spectrum of potential health effects associated with VOC exposure is vast and includes sensory and chemosensory outcomes (odor perception and perceived air quality), mucosal irritation (eyes, nose, throat), allergic manifestations, respiratory morbidity, and, for certain compounds, carcinogenic outcomes. However, elucidating causal relationships between indoor VOCs and adverse health outcomes is generally more complex than for outdoor air pollution. A principal challenge is that exposure typically involves dynamic mixtures of chemically diverse VOCs cooccurring with other indoor contaminants (e.g., ozone, nitrogen oxides, particulate matter), and empirical knowledge regarding toxicological interactions, synergisms, and combined effects remains limited. The biological mechanisms underlying VOC-related health effects depend strongly on molecular structure, physicochemical properties, and reactivity. Accordingly, the VOC class encompasses compounds with widely heterogeneous toxicological profiles, ranging from relatively inert species with no established adverse effects at typical indoor concentrations to highly reactive compounds capable of eliciting clinically relevant responses. [28]

In general, potential health impact associated with exposure to VOCs are commonly organized into two domains:

- non carcinogenic risks
- carcinogenic risks.

Early controlled exposure studies conducted in the 1980s, often employing chamber experiments with mixtures representative of building related emissions, reported acute symptoms such as headache and irritation at concentrations in the mg/m^3 range. Subsequent experimental syntheses have indicated symptom thresholds for endpoints such as odor, perceived air quality, and ocular or upper airway irritation spanning approximately 1.7–25 mg/m^3. These concentrations are generally higher than those typically observed in residential and office environments, suggesting that extrapolation from high dose chamber experiments to real world indoor exposures requires careful interpretation. [27]

Beyond transient sensory irritation, increasing scientific evidence indicates that exposure to volatile organic compounds (VOCs) in indoor environments is associated with adverse respiratory outcomes, particularly among vulnerable subpopulations such as infants, young children, and individuals with atopic predisposition. These groups may exhibit heightened biological susceptibility due to ongoing lung development, immature immune responses, or preexisting inflammatory conditions affecting the airways. [29]

A number of epidemiological and observational studies have identified significant associations between indoor concentrations of specific VOCs, including benzene, toluene, xylenes, styrene, dichlorobenzenes, and ethylbenzene, and a range of respiratory symptoms. Reported effects encompass persistent cough, wheezing, airway irritation, recurrent respiratory infections, nocturnal dyspnea, and measurable reductions in lung function parameters such as forced expiratory volume and peak expiratory flow. In some cases, exposure has also been linked to increased bronchial hyperresponsiveness and exacerbation of asthma related symptoms. [30]

Although the precise biological mechanisms remain under investigation, proposed pathways include airway epithelial irritation, oxidative stress, inflammatory responses, and modulation of immune function. Importantly, indoor environments often contain complex mixtures of VOCs rather than single compounds, complicating the attribution of observed health effects to individual substances. Nonetheless, cumulative evidence supports the

conclusion that chronic or repeated exposure to indoor VOCs may contribute meaningfully to respiratory morbidity, especially in populations with increased vulnerability. [31]

Formaldehyde merits particular attention due to its ubiquity in indoor environments and its intrinsic chemical reactivity. As an efficient airway irritant, formaldehyde is readily deposited and absorbed in the respiratory tract and can react with biological macromolecules. Multiple studies have reported relationships between indoor formaldehyde concentrations and asthma-like symptoms, wheeze, and atopic outcomes, with some evidence suggesting dose–response patterns across exposure ranges that are not uncommon in residential settings. [32]

It is imperative to mention Carbon Monoxide, one of the most harmful and common VOC, detectable easily in a wide range of daily contexts, from domestic to working environments. CO is an odorless, colorless, and highly toxic gas produced by the incomplete combustion of carbon containing materials. It represents one of the leading causes of fatal poisoning worldwide, accounting for more than half of reported poisoning deaths in many countries. However, mortality and morbidity data are likely underestimated due to frequent under reporting and misdiagnosis, making the true prevalence of CO intoxication difficult to determine. The clinical effects of CO exposure vary according to concentration and duration. At low levels, exposure may result in subtle cardiovascular and neurobehavioral alterations, whereas higher acute or chronic exposures can lead to loss of consciousness and death. Immediate mortality is typically cardiac in origin, reflecting the high sensitivity of myocardial tissue to hypoxic injury. Advanced poisoning may cause profound hypotension, malignant arrhythmias, electrocardiographic abnormalities, and pulmonary edema. Neurological involvement includes confusion, disorientation, and coma. A particularly concerning consequence is delayed neuropsychiatric syndrome, which may develop from days to weeks after exposure and resolve only gradually. CO exposure during pregnancy poses substantial risks, increasing maternal complications and potentially resulting in fetal death, developmental abnormalities, or chronic neurological damage.[33], [34], [35]

A subset of VOCs presents concerns related to mutagenicity and carcinogenicity. Carcinogenic effects concern VOCs with evidence of cancer initiation or promotion following chronic exposure. Several VOCs present in indoor and outdoor air, most prominently benzene, formaldehyde, and some chlorinated hydrocarbons, are classified as known or suspected human carcinogens. In general, cancer risk reflects not only contemporaneous concentration but also cumulative exposure over time, as well as potential interactions with cooccurring pollutants. [36]

Carcinogenicity assessment is methodologically complex and is typically grounded in converging evidence from long term animal studies and epidemiological investigations, with additional support from structure–activity relationships and short-term genotoxicity assays. Under the International Agency for Research on Cancer (IARC) framework, substances are categorized according to the weight of evidence as carcinogenic, probably carcinogenic, or possibly carcinogenic to humans. Within this system, formaldehyde, benzene, and vinyl chloride are classified as human carcinogens, while compounds such as 1,3-butadiene, benzyl chloride, tetrachloroethylene, and trichloroethylene have been categorized as probable human carcinogens. IARC's evaluation of formaldehyde (classified as carcinogenic to humans in 2004) emphasizes sufficient evidence for nasopharyngeal cancer, limited evidence for sinonasal cancers, and strong, though not sufficient, evidence for leukemia. [30], [31]

Figure 1.5 provides a schematic overview of the principal health effects associated with exposure to VOCs. The diagram synthesizes the range of adverse outcomes reported in scientific literature and highlights those effects for which there is consistent epidemiological and toxicological evidence:

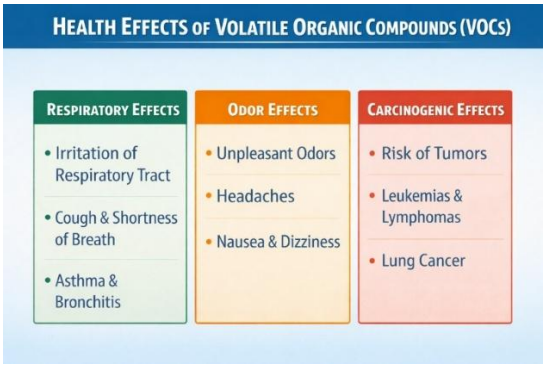

Figure 1.5. Documented Health effect of VOCs.

Particularly in indoor environments, a thorough examination of the regulatory framework governing human exposure to VOCs is essential. Indoor settings may present elevated exposure risks due to limited ventilation, the presence of multiple emission sources, and prolonged occupancy times. Consequently, occupational and environmental regulations play a critical role in defining acceptable exposure thresholds and safeguarding human health. [37]

Within this context, reference should be made to the Permissible Exposure Limits (PELs) established by the Occupational Safety and Health Administration (OSHA) in the United States. OSHA defines, for a broad range of VOCs and other hazardous substances, an 8-hour Time Weighted Average (TWA) Permissible Exposure Limit. The 8-hour TWA PEL represents the maximum average concentration of a substance to which a worker may be exposed during a standard work shift without a significant risk of adverse health effects, based on available toxicological and epidemiological evidence. [38]

The TWA approach accounts for fluctuations in exposure over time by averaging concentrations across the workday, thereby providing a more realistic assessment of occupational risk than instantaneous measurements. These regulatory limits constitute a key instrument in occupational health protection, guiding risk assessment, workplace monitoring, and the implementation of preventive measures aimed at minimizing harmful exposure to VOCs and other airborne contaminants. Table 1.3 presents the regulatory exposure limit values established for selected volatile organic compounds of particular toxicological relevance.

Compound	8-hour TWA PEL
Acetaldehyde	25 ppm
Benzene	1 ppm
Acetone	3000 ppm
Carbon monoxide	25 ppm
Xylenes	300 ppm
Formaldehyde	2 ppm
Total dust	10 mg/m^3

Table 1.3. 8-hour TWA PEL of VOC, modified from www.osha.org.

1.5 Solutions for VOCs Abatement

In response to progressively stricter regulations governing VOCs emissions, considerable efforts have been undertaken to develop effective abatement strategies. The need to mitigate the environmental and health impacts associated with VOCs, particularly their contribution to atmospheric pollution and indoor air quality deterioration, has significantly advanced research in this domain. VOC removal technologies can be systematically categorized into two principal groups: capture methods and destruction methods. Recovery approaches are designed to separate VOCs from contaminated air streams while preserving their chemical structure, thereby allowing potential reuse or safe handling. In contrast, destruction methods aim to chemically convert VOCs into less harmful substances, typically through oxidation processes that yield carbon dioxide and water as end products. [39]

Technologies based on VOC recovery include:

- Absorption in liquid solutions, where VOCs are transferred from the gaseous phase to a liquid medium based on solubility and mass transfer principles. In this process, VOCs are transferred from the gas phase into a liquid phase, typically water or an organic solvent, based on solubility and mass transfer principles. This method is especially suitable for high concentration streams and compounds with favorable solubility characteristics. [40]
- Adsorption onto solid materials, such as activated carbon and zeolites. This approach primarily involves electrostatic interactions, affinity between polar compounds and hydrophilic sites, interactions between nonpolar compounds and hydrophobic domains. Adsorption performance typically increases with greater specific surface area, larger pore volume, enhanced surface functionalization, and reduced pore size. Consequently, the selection of appropriate adsorbent and operating conditions depends on both the physicochemical properties of the target VOC and the structural and chemical characteristics of the adsorbent material.[41], [42]
- Condensation, particularly suited for treating high concentration emission streams. This process utilizes liquid refrigerants to facilitate a phase transition, effectively transforming VOC vapors into a recoverable liquid state by systematically reducing the emission stream's temperature, increasing its pressure, or employing a combination of both thermodynamic mechanisms. [43]
- Membrane separation, that exploits selective permeability to separate VOCs from air streams. Their advantages include modular design, relatively low energy requirements, and the absence of phase change, although membrane fouling and selectivity limitations remain technical challenges. [44]

Conversely, methods based on the chemical destruction of VOCs include:

- Thermal oxidation, which involves the degradation of VOCs at high temperatures, typically above 700–800 °C, converting them into carbon dioxide and water. While highly effective, thermal incineration is energy-intensive and may require heat recovery systems to improve overall efficiency. [45]
- Catalytic oxidation, that enables VOC oxidation at significantly lower temperatures compared to thermal incineration, thereby reducing energy consumption. The presence of a catalyst lowers the activation energy of the reaction, enhancing efficiency and making this technique particularly attractive for continuous treatment applications.[46]

- Biodegradation, that employs microorganisms to metabolize VOCs, converting them into harmless byproducts. Most used methods include biofilters, bio trickling filters, increasingly recognized as cost effective and environmentally sustainable technologies for the removal of VOCs from industrial emissions. [47]
- Photocatalysis, in which light activated catalysts, commonly titanium dioxide (TiO_2), are employed to generate reactive species capable of oxidizing VOCs under mild operating conditions. This technique has gained attention for indoor air purification due to its potential for low temperature operation and its cost effectiveness.[48]
- Plasma technologies, which utilize reactive species generated in non-thermal plasma to decompose organic pollutants. Plasma, a partially ionized gas composed of energetic electrons, ions, and reactive species, enables chemical reactions to occur while the bulk gas remains near ambient temperature. This technology may involve operational complexity, challenges related to energy efficiency, and the formation of secondary byproducts, which require careful control and optimization. [49]

The selection of an appropriate VOC abatement technology depends on several factors, including pollutant concentration, chemical composition, air flow rate, economic constraints, and regulatory requirements. A comprehensive evaluation of these parameters is essential to ensure both technical feasibility and environmental sustainability.[39]

1.6 Catalytic Oxidation

Catalytic oxidation represents a widely adopted strategy for the abatement of volatile organic compounds (VOCs), enabling their conversion into carbon dioxide and water. In contrast, conventional thermal incineration, although effective, requires high operating temperatures and substantial energy input, and may generate toxic byproducts. For this reason, catalytic oxidation has emerged as one of the most effective and economically viable technologies for VOC removal, as it promotes the complete destruction of pollutants rather than transferring them to another phase, as occurs in condensation or adsorption processes. [50]

In catalytic oxidation, VOCs react in the presence of an appropriate catalyst at significantly lower temperatures, typically between 250 and 500 °C, compared with non-catalytic thermal oxidation. This lower operating temperature improves thermal efficiency and reduces fuel consumption, particularly when the process is integrated with heat recovery systems such as recuperative heat exchangers. As a result, catalytic combustion is especially suitable for treating moderate volumes of contaminated air containing low VOC concentrations, typically below 1%. Under these conditions, the process offers reduced operating costs, lower startup fuel requirements, and improved overall energy efficiency. [51]

Despite these advantages, several challenges remain. One of the main limitations is the selection of suitable catalysts from the wide range of available materials. Although VOC oxidation is an exothermic reaction, the overall process still requires energy input, especially at low pollutant concentrations, since the entire gas stream must be heated to elevated temperatures, often exceeding 200 °C. This requirement increases operational costs and introduces safety concerns, including the risk of explosion and the formation of secondary pollutants such as NOx. In addition, prolonged exposure to high temperatures may lead to catalyst sintering and deactivation. [52]

For these reasons, considerable research efforts have focused on developing catalysts capable of operating efficiently at lower temperatures, ideally near ambient conditions, in order to improve safety, reduce energy consumption, and enhance environmental compatibility. However, real industrial gas streams often contain additional contaminants such as water vapor, ammonia, sulfur compounds, and organ halogens, which can poison conventional oxidation catalysts, including supported platinum and nickel systems. Therefore, catalysts used for VOC oxidation must combine high activity, low selectivity toward undesired by-products, and strong resistance to deactivation.[51]

In general, catalytic performance depends strongly on several factors, including catalyst composition, preparation method, metal loading, particle size, and support characteristics. In addition, operating conditions such as VOC concentration, oxygen availability, gas flow rate, and reactor configuration also play a critical role. Both noble metals and transition metal oxides have been extensively studied for the oxidation of halogenated and nonhalogenated VOCs; however, noble metal catalysts remain the preferred choice in many applications due to their superior activity and durability. [53]

As a matter of fact, noble metal catalysts, particularly platinum-based formulations, have demonstrated superior performance due to their high intrinsic activity, stability, and regenerability, despite their higher cost. The enhanced performance was attributed to increased lattice oxygen mobility and the ability of the support material to provide reactive oxygen species even below 100 °C, which significantly accelerates oxidation reactions. [54]

Focusing on the support materials, among the most widely employed solutions are zeolites and metal oxides, owing to their favorable physicochemical properties and structural versatility.

Zeolites are crystalline, microporous and/or mesoporous aluminosilicate minerals characterized by a well-defined three-dimensional framework composed of interconnected SiO_4 and AlO_4 tetrahedra. These primary building units share oxygen atoms to form an extended lattice containing uniform channels and cages with dimensions typically in the nanometer range. [55]

An example of silicate commonly used in catalytic oxidation is the SBA-15, a mesoporous silica developed by researchers at the University of California at Santa Barbara. It is characterized by a highly ordered hexagonal arrangement of uniform mesopores, with tunable pore diameters typically ranging from 5 to 15 nm and a narrow pore-size distribution. A key feature of SBA-15 is its relatively thick pore walls (approximately 3.1-6.4 nm), which confer enhanced hydrothermal and mechanical stability compared to many other mesoporous silicas. Owing to its large specific surface area and well-defined porous structure, SBA-15 is widely applied in environmental adsorption and separation processes, advanced optical systems, and heterogeneous catalysis[56]. The structure of this support is depicted in the Figure 1.6.

Figure 1.6. Schematic structure of SBA-15, modified from [57]

In the class of aluminosilicate support, an important role is given to microporous zeolite. This ordered microporous architecture confers high specific surface area and significant adsorption capacity, making zeolites particularly suitable for applications involving the capture and transformation of VOC molecules. In addition, their synthesis can be precisely controlled, allowing for reproducible structural and compositional properties, while their intrinsic thermal stability enables operation under the elevated temperatures typical of catalytic oxidation processes [58].

A fundamental property of zeolites relevant to catalytic applications is their acidity. The incorporation of aluminum into the silica framework generates a negative charge imbalance, which is compensated by external framework cations. When protons serve as charge-compensating species, Brønsted acid sites are formed. These sites act as proton donors and play a central role in acid catalyzed reactions. In parallel, Lewis acid sites, defined as electron pair acceptors, may also be present, either inherently or as a result of structural modifications. The coexistence of Brønsted and Lewis acid sites enables a range of adsorption and activation mechanisms for VOC molecules, influencing both reaction pathways and selectivity. [59]

Thermal treatment significantly affects the acidic properties of zeolites. Under severe heating conditions (e.g., around 500 °C), dehydroxylation may occur, leading to the degradation of Brønsted acid sites. This process involves the removal of hydroxyl groups from the framework and is often accompanied by the generation of additional Lewis acid sites. Such transformations modify the acid site distribution and strength, thereby altering catalytic behavior. Consequently, understanding and controlling the acid characteristics of zeolitic supports is essential for optimizing their performance in VOC catalytic oxidation systems. [58]

Even though zeolites have been extensively investigated as supports for the catalytic oxidation of VOCs, metal oxides represent a highly relevant and often more robust class of supports for the previously cited aim. In comparison with microporous supports, crystalline oxide carriers generally exhibit a lower susceptibility to deactivation associated with pore blockage: because they are typically non-microporous, they are less prone to the accumulation of carbonaceous deposits (coke) within confined channels, which can otherwise hinder mass transfer and progressively mask active sites. [52]

Among the most common non-porous or low-porosity oxide supports employed in oxidation catalysis are TiO_2, SiO_2, and ZrO_2.These materials are valued for their thermal stability, mechanical resistance, and chemical inertness (particularly SiO_2), as well as for their ability to stabilize metal nanoparticles and modulate metal–support interactions (notably TiO_2 and ZrO_2). Such interactions can influence key catalyst properties including metal dispersion, redox behavior at the interface, and resistance to sintering under the high-temperature, oxidizing environments typical of VOC abatement processes. [58]

A particularly important oxide support is cerium dioxide (CeO_2, ceria), widely used in automotive three-way catalysts and increasingly adopted in VOC oxidation systems because of its exceptional redox properties. Ceria can reversibly cycle between Ce^{4+} and Ce^{3+} states, enabling the formation and healing of oxygen vacancies and conferring a significant oxygen storage/release capacity. Under oxidizing conditions, CeO_2 can uptake oxygen and replenish its lattice, whereas under reducing conditions it can release oxygen to sustain oxidation reactions locally. This oxygen buffering function is crucial in applications characterized by transient or fluctuating feed compositions, and it can enhance catalytic

activity by facilitating oxygen transfer to the active metal phase and promoting sustained oxidation at the metal-oxide interface. [60]

In terms of structure, Ceria exhibits a fluorite crystal structure, characterized by a face-centred cubic lattice with a space group $Fm\bar{3}m$. The lattice parameter is approximately 5.411 Å. In this arrangement, Ce^{4+} cations occupy the corners and the center of the cubic unit cell, forming a cubic close-packed sublattice. Oxygen anions fill all tetrahedral interstitial sites, leading to the characteristic coordination environment of the fluorite phase: each Ce^{4+} ion is eightfold coordinated by O^{2-} ions in a cubic geometry, whereas each oxygen ion is tetrahedrally coordinated by four cerium ions. The unit cell therefore consists of a periodic three-dimensional network of these coordination polyhedra, which repeats throughout the crystal and defines the long-range order of CeO_2. [61]

The figure 1.7 shows the crystal structure of CeO_2:

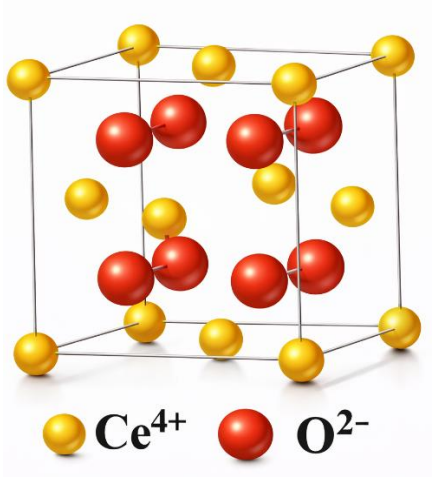

Figure 1.7. Fluorite Structure of Cerium dioxide, modified from [62].

Among catalysts based on noble metals, a wide range of effective formulations has been investigated and reported in the literature. The noble metals most frequently employed for oxidation and combustion applications include platinum (Pt), ruthenium (Ru), silver (Ag), and gold (Au), owing to their favorable redox properties and their ability to promote oxygen activation on the catalyst surface. Within this class, Pt-based catalysts are widely recognized as particularly effective for the catalytic combustion of cyclic hydrocarbon compounds. They also demonstrate high activity toward the oxidation of BTEX species (benzene, toluene, ethylbenzene, and xylenes), typically exhibiting appreciable conversion in the temperature interval of approximately 150-350 °C. Consistently, it has been reported that Pt/CeO_2 catalysts exhibit enhanced oxygen storage capacity and improved reducibility relative to bare CeO_2, leading to superior catalytic performance in VOC combustion. This improvement is commonly attributed to synergistic metal–support interactions that increase the availability of reactive oxygen species and promote more efficient oxidation pathways at lower temperatures [63]

It is important to go into details analyzing two relevant mechanism of reactions, associated to two volatile compounds of interest: carbon monoxide (CO) and ethylene (C_2H_4). Carbon monoxide, as previously cited, is a toxic product of incomplete combustion, while ethylene is a stable hydrocarbons, very challenging to oxidize at low temperature. CeO_2–Pt catalysts can attain high CO conversion at much lower temperatures than conventional Pt/Al_2O_3. In

the literature many studies focused on the explanation of why Pt/CeO_2 is so active for CO oxidation[64].

Two main effects emerge:

- Electronic and oxygen donation effects from the CeO_2 support;
- Pt nuclearity (dispersion) effects.

In the cooperative mechanism, the CeO_2 support supplies lattice oxygen to oxide CO adsorbed on Pt; subsequently, the reduced ceria is rapdly reoxidized by molecular oxygen from the gas phase. This process follows a Mars–van Krevelen cycle occurring at the metal–oxide interface. This mechanism is supported by experimental evidence showing that CO oxidation rates often scale with the number of Pt–CeO_2 interfacial sites. In particular, highly dispersed Pt, characterized by a larger fraction of perimeter atoms, exhibit higher activity per Pt atom compared to larger Pt particles. Density functional theory calculations and in situ spectroscopies studies have demonstrated that CO adsorbs on Pt and abstract an oxygen atom from the ceria lattice, leading to the formation of CO_2 and leaving behind a oxygen vacancy in the ceria structure. This vacancy is subsequently refilled by gas-phase O_2, completing the catalytic cycle. This synergistic interaction indicates that the active site consists of a Pt–CeO_2 ensemble: CO adsorbs on Pt, O_2 is activated on the ceria surface (as a lattice oxygen or a superoxide species), and the close proximity of Pt and CeO_2 lowers the activation barrier for CO oxidation. [65]

For Ethylene, a similar mechanism can be proposed, involving two main pathways:

- Catalytic oxidation with gaseous oxygen, which involves the direct reaction between activated molecular oxygen adsorbed on the catalysts surface and ethylene;
- Electrochemical oxidation involving lattice oxygen, in which oxygen species originating from the catalyst support participate directly in the reaction. In this pathway, lattice oxygen ions migrate to the three-phase boundary, where they react with ethylene. This process is accompanied by the release of electrons and is associated with a change in the oxidation state of the support material, particularly cerium oxide, which undergoes partial reduction during the reaction [66]

The present mechanisms help to understand better the oxidations of the two representative pollutants chosen in this work. The latter focuses indeed on the investigation of the catalytic oxidation carbon monoxide, and ethylene, selected as a representative VOC to evaluate catalyst performance in terms of hydrocarbons oxidation.

An important aspect to consider in catalyst design is the economic feasibility associated with the incorporation of noble metals. noble metals such as platinum, palladium, and rhodium exhibit outstanding physicochemical properties, including:

- high resistance to oxidation and corrosion
- remarkable thermal stability
- chemical inertness acidic conditions
- elevated electrical conductivity
- excellent mechanical workability

These intrinsic properties make them highly attractive for a broad range of industrial applications, including heterogeneous catalysis, electronics, automotive emission control systems, and energy conversion technologies. However, noble metals are among the rarest

elements in the Earth's crust, with typical concentrations on the order of parts per billion. Their extraction requires complex mining and refining processes, often associated with significant energy consumption and environmental impact. As a consequence of their scarcity and the technical challenges involved in their production, their availability is structurally limited. [67]

Furthermore, the market price of noble metals is highly volatile and strongly influenced by multiple external factors. In addition to intrinsic scarcity, supply–demand imbalances play a central role. Demand is largely driven by key industrial sectors, particularly automotive catalysis, chemical manufacturing, and emerging clean-energy technologies, while supply is geographically concentrated in a limited number of countries. This geographic concentration exposes the market to geopolitical instability, trade policies, regulatory constraints, and fluctuations in mining output and technological efficiency. [68]

As a result, the development of catalytic systems that minimize noble metal loading while preserving high activity and stability represents a major research objective. Strategies such as enhanced metal dispersion, strong metal–support interactions, alloy formation, and the use of redox-active supports are increasingly explored to optimize catalytic performance while improving overall economic sustainability. [69]

Figure 1.8 shows the fluctuations in the market price of Platinum. The period analyzed is between 2000 and 2026. It is clear that the trend is increasing in the last years. The elevated current prices of noble metals can be attributed to the combined effects of constrained supply, increasing industrial demand, strategic stockpiling practices, and their intrinsic geological scarcity. These factors operate within a highly sensitive and globally interconnected market, in which even relatively small fluctuations in production capacity or consumption levels can generate significant price volatility. The structural imbalance between limited primary extraction sources and expanding technological applications further amplifies this economic instability.

Figure 1.8. Market price of Platinum in the last 26 years, modified from www.macrotrends.net.

Given the previously cited factors, extensive research has sought to optimize the concentration of noble metals incorporated into catalytic systems. While the ideal quantity varies according to the specific rare element utilized, existing literature suggests an effective range between 0.2% and 2.5% by weight. [70]

Another critical aspect concerns the relationship between specific surface area and catalytic performance. Numerous studies have highlighted that catalysts with higher specific surface areas generally exhibit superior activity because they provide a greater number of accessible active sites for reactant adsorption. Since catalytic reactions occur at the surface of the material, the availability of these sites directly influences the reaction rate, overall efficiency, and, in many cases, the selectivity toward desired products. An increased surface area enhances the probability of effective interactions between reactant molecules and active centers, thereby facilitating adsorption, surface reaction, and subsequent desorption of products. [71]

High surface areas are typically achieved through the use of highly porous supports, which contain extensive networks of micro, meso, or macropores. These porous structures significantly increase the internal surface area, which often represents the dominant contribution compared with the external surface. As a result, porous support enables a more uniform dispersion of the catalytically active phase and promote a higher density of exposed active sites. This is particularly relevant for noble metal catalysts, such as platinum, where maximizing metal dispersion is essential to optimize metal utilization and catalytic efficiency. In this context, reducing the crystallite size of the active phase increases the fraction of atoms located at the surface relative to those in the bulk, thereby enhancing catalytic performance. Similarly, increasing the porosity of the support improves accessibility to internal active sites and facilitates mass transport of reactants and products. [72], [73]

The specific surface area also plays a crucial role in determining catalytic stability. Catalysts with higher surface areas generally possess a greater capacity to accommodate carbonaceous deposits, such as coke, by distributing them over a larger surface. This distribution reduces the likelihood of complete blockage of active sites and pore channels. Conversely, catalysts with lower specific surface areas are more susceptible to rapid deactivation because even small amounts of coke can block a significant fraction of the available active sites. This blockage restricts reaction access and accelerates the loss of catalytic activity. Therefore, optimizing the surface area and porosity is essential not only to enhance catalytic activity but also to improve catalyst durability and resistance to deactivation under operating conditions. [74], [75]

The present dissertation aims to enhance the catalytic activity and stability of Pt/CeO_2 catalysts through the structural optimization of the support's specific surface area. The noble metal loading has been kept constant at 0.5 wt.% Pt, a concentration deliberately selected to ensure a highly dispersed active phase, thereby guaranteeing optimal catalytic performance while maintaining cost-effectiveness.

2. Experimental section

In this section, the experimental part of this dissertation will be examined in detail, beginning with a description of the synthesis procedures adopted for the preparation of the employed catalysts. Particular attention will be given to the reagents, experimental conditions, and methodological steps that were followed to obtain the desired materials. Subsequently, the characterization methods used to investigate the physicochemical properties of the synthesized catalysts will be presented and discussed, with the aim of providing a comprehensive understanding of their structural and compositional features. Finally, the experimental tests conducted on the samples will be described, outlining the testing procedures, operating conditions, and evaluation criteria adopted to assess their performance. This systematic approach allows for a clear correlation between synthesis, characterization, and catalytic behavior, supporting the interpretation of the obtained results.

2.1 Catalyst preparation

In the catalyst preparation workflow, the first step consisted in synthesizing the oxide support. In particular, three cerium dioxide (CeO_2) supports with different textural properties were prepared using cerium nitrate hexahydrate ($Ce(NO_3)_3 \cdot 6H_2O$) as the cerium precursor:

- CeO_2 Low surface area, indicated as CeO_2 LSA
- CeO_2 Medium surface area, indicated as CeO_2 MSA
- CeO_2 High Surface Area, indicated as CeO_2 HSA

For the first two supports, namely CeO_2 LSA and CeO_2 MSA, the synthesis was carried out via solution combustion synthesis (SCS), a rapid route in which an oxidizing metal nitrate and a fuel (here, urea) react exothermically to yield the corresponding oxide. Following the methodology reported by Andana and Piumetti, the procedure was implemented as described below.

First, two precursor solutions were prepared independently. In the first case, 1.9041 g of $Ce(NO_3)_3 \cdot 6H_2O$ and 0.900 g of urea were dissolved in 30 mL of distilled water under stirring until complete dissolution. In the second case, an analogous preparation was performed using 1.9081 g of $Ce(NO_3)_3 \cdot 6H_2O$ and 0.905 g of urea, again dissolved in 30 mL of distilled water. Subsequently, the resulting solutions were transferred into crucibles and subjected to thermal treatment at 600 °C for 2 h. Under these conditions, the combustion reaction and subsequent calcination promoted solvent removal and decomposition of nitrate species, ultimately producing solid CeO_2 powders at high superficial area, whose macroscopic appearance is showed in Figure 2.1. [76], [77]

Figure 2.1. Ceria Powder.

For completeness, the synthesis was also repeated by varying the amount of distilled water used for dissolution (30 mL vs. 60 mL) in order to evaluate whether the solvent volume influences the final specific surface area. However, BET measurements performed on the obtained powders indicated no observable correlation between the initial water volume and the resulting surface area within the investigated conditions, as it will be noted later in the characterization section.

One of the obtained CeO_2 powders was then calcinated at 900°C in an oven, in order to reduce superficial area and obtain the CeO_2 Low superficial Area (CeO_2 LA). In fact, the high temperature of calcination lead to destruction of the support textural properties and subsequent collapse of mesopores, resulting into the decrease in surface area. [78]

A different synthesis technique was selected for the support named CeO_2 HSA. In accordance to the procedure proposed by Ballauri, a solution formed by 7.6 g of $Ce(NO_3)_3 \cdot 6H_2O$ was prepared by dissolving the salt in 25 mL of ethanol under magnetic stirring until complete solubilization. Subsequently, 1.0 g of SBA-15 was introduced into 15 mL of the resulting precursor solution, and the suspension was stirred at room temperature for 1 h to promote the infiltration of the cerium containing species into the mesoporous silica framework.

After the impregnation step, the solvent was removed by evaporation at 60 °C using a heating plate, yielding a dry impregnated solid. To ensure a more complete pore filling and improve precursor loading within the SBA-15 channels, the impregnation/evaporation procedure was repeated using the remaining precursor solution. Finally, the obtained material was subjected to calcination at 500 °C for 2 h to decompose the nitrate precursor and generate the corresponding cerium oxide phase within the SBA-15 template. In this way, the support entitled CeO_2 HSA was obtained. [79]

The subsequent phase involved the synthesis of platinum nanoparticles. Following the procedure proposed by Wang and Chen, an appropriate amount of chloroplatinic acid hexahydrate ($H_2PtCl_6 \cdot 6H_2O$), corresponding to a platinum content of 8 wt.%, was dissolved in 20 mL of ethylene glycol to obtain the first precursor solution. In parallel, a second solution was prepared by dissolving 0.22 g of NaOH in 20 mL of ethylene glycol. This alkaline solution was then added dropwise to the precursor solution under continuous stirring, and the mixture was maintained under agitation for 1 h at room temperature to ensure homogeneous conditions.

Afterwards, the resulting mixture was heated to 90 °C and kept under stirring for 2 h. Throughout this thermal treatment, a continuous nitrogen (N_2) bubbling flow was introduced into the system to promote an inert atmosphere and to facilitate the removal of water and volatile byproducts formed during the reduction process. A schematic representation of the experimental setup adopted for this step is reported in Figure 2.2. [73], [80]

Figure 2.2. Reaction system for system and heating of the solution of Chloroplatinic Acid Hexahydrate, NaOH and EG for Pt nanoparticles synthesis.

After the reaction mixture was allowed to cool to room temperature, a stoichiometric amount of 0.3 M hydrochloric acid (HCl) was added in order to neutralize the residual base and to promote the quantitative formation of sodium chloride (NaCl) as a precipitate. This step was carried out to remove excess NaOH and to stabilize the suspension prior to further processing. [73]

Afterwards, an ethanolic solution containing 40 mg of polyvinylpyrrolidone (PVP) was introduced. PVP is a stabilizing polymer for noble-metal colloids, as it can adsorb on the nanoparticle surface and favor nucleation while limiting uncontrolled aggregation. In particular, the aliphatic segments of the polymer chains can modulate the interfacial environment and affect the mass transport of precursor ions and reduced species toward the growing Pt nuclei. As a result, PVP contributes to regulating the growth kinetics and, consequently, to controlling the final particle size distribution. [81]

To ensure homogenization, the suspension was subjected to vortex mixing for 1 min, leading to complete dispersion of the nanoparticles. Finally, the prepared Pt nanoparticles were characterized by transmission electron microscopy (TEM) to estimate their mean particle size and assess the morphology; these results are discussed in a subsequent section.

After the preparation of nanoparticles solution, three final samples were prepared, named:

- Pt/CeO_2 Low Surface Area, indicated as Pt/CeO_2 LSA
- Pt/CeO_2 Medium Surface Area, indicated as Pt/CeO_2 MSA
- Pt/CeO_2 High Surface Area, indicated as Pt/CeO_2 HSA

The three samples were synthesized in accordance to the same procedure proposed by Chen. More specifically, 50 mL of Ethanol was used to dissolve 1g of CeO_2 LSA, CeO_2 MSA and CeO_2 HSA in three different backers. Then, 8 mL of the solution of Platinum nanoparticles was added in all the Beckers. The resulting solutions, showed in Figure 2.3, were stirred at room temperature for 24 hours to promote the deposition of Pt nanoparticles onto the ceria surface. After the stirring, the solutions were submitted to centrifugation in order to separate solid phase from liquid one. The wash-centrifugation cycle was conducted until the liquid phase reached a neutral pH (equal to 7). The recovered wet solid phases was finally

transferred into ceramic crucibles and submitted to a 12 hours thermal treatment into an oven at 350°C, obtaining thereby the final samples. [73]

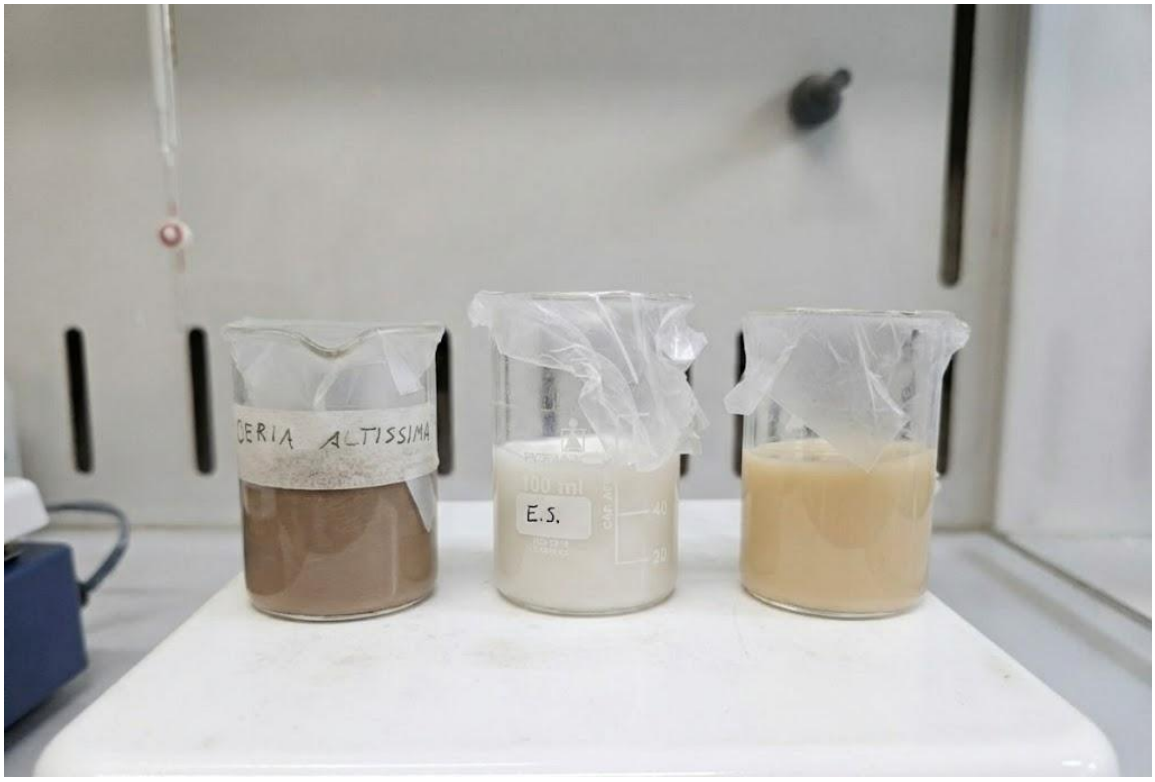

Figure 2.3. Solutions of Pt nanoparticles and cerium supports.

2.2 Characterization techniques

Catalyst characterization is a central and persistent challenge in chemical catalysis, because it provides the experimental basis for linking material structure to catalytic performance and, ultimately, for catalyst design. A comprehensive characterization strategy must consider both physical and chemical properties, since catalytic behavior typically emerges from the interplay between textural features (e.g., surface area and porosity), structural attributes (e.g., crystallinity and phase composition), and chemical characteristics (e.g., oxidation state, reducibility, and surface site nature).

For porous materials, characterization is primarily aimed at describing the architecture of the pore network, which strongly influences mass transport, adsorption, and accessibility of reactants to active sites. Key parameters include the total pore volume, the pore diameter, and the pore size distribution, as well as the degree of pore connectivity. These descriptors are essential for interpreting diffusion limitations and for distinguishing between micro, meso, and macroporous contributions, each of which can affect catalytic activity and selectivity in different ways.

In the case of noble-metal catalysts, and in particular platinum-based systems, additional emphasis is placed on quantifying the metal dispersion and the structural features of the supported metal nanoparticles. Because catalytic activity often scales with the number of accessible surface atoms, it is crucial to estimate the mean particle size of the dispersed metal phase and to determine the size distribution of the nanoparticles rather than relying solely on average values. Closely related objectives include the determination of platinum dispersion and the estimation of the exposed active metal surface area, which together provide an operational measure of the fraction of metal atoms available to participate in surface reactions.

Equally important is the investigation of the redox properties of both the metal phase and the support. This aspect becomes particularly relevant for oxidation catalysis proceeding through the Mars–van Krevelen mechanism, where the support (or lattice oxygen) can take an active role in the reaction cycle and where catalyst performance depends on the balance between oxygen donation and subsequent reoxidation. In this context, determining reducibility, oxygen mobility, and the stability of oxidation states is essential to interpret activity trends and to identify rate- or selectivity-determining steps. Beyond these core targets, catalyst characterization commonly aims:

- identifying the crystalline structure and phase composition of the material, including potential metal-support interfacial phases.
- examining particle morphology and the spatial distribution of metal nanoparticles on the support.
- analyzing the nature, type, and strength of active sites, including distinctions between metallic sites, partially oxidized sites, and interfacial sites.

In this paragraph, all the techniques used for the characterization will be discussed, with particular attention to the physical principles behind their functioning and their specific aims.

2.2.1 BET Nitrogen physisorption

Brunauer–Emmett–Teller (BET) analysis is a technique based on the homonymous theory, used to characterize the structure of a porous material and able to quantify its specific surface area through the adsorption of a gas on the solid surface. The BET theory, introduced in 1938, was developed as an extension of the Langmuir adsorption model. While the Langmuir theory is well suited to relatively simple systems under near-ideal conditions, typically assuming an adsorbate behaving as an ideal gas under isothermal conditions, it relies on a set of restrictive assumptions that limit its applicability. In particular, Langmuir adsorption is based on the concept of monolayer formation on a homogeneous surface. The main assumptions of the Langmuir model can be summarized as follows:

- Monolayer coverage: each adsorption site can accommodate at most one adsorbate molecule.
- Saturation at monolayer completion: adsorption cannot proceed beyond the formation of a single, complete monolayer (i.e., a maximum adsorption capacity is reached).
- Energetic equivalence of sites: all surface sites are considered identical from an energetic standpoint, meaning they share the same adsorption enthalpy and therefore the same probability of being occupied; the surface is assumed to be microscopically uniform and ideally flat.
- Negligible lateral interactions: adsorbate–adsorbate interactions are assumed to be insignificant compared with adsorbate–adsorbent interactions, implying a constant adsorption energy independent of surface coverage.
- Reversibility and immobility: adsorption is treated as a reversible process, and adsorbed molecules are often assumed not to migrate along the surface.
- Activity with concentration approximation: under sufficiently dilute conditions, the activity of the adsorbate, a function that quantifies the deviation from ideality, can be approximated by its concentration (or, in the gas phase, by partial pressure expressed in concentration-like form).

The BET theory extends the description to multilayer adsorption, thereby offering a more realistic representation for many non-reactive gas-solid systems. BET analysis is typically performed using gases that do not chemically react with the solid, so that adsorption is predominantly physical (van der Waals) in nature. The model is built on the following idealized assumptions:

- Layer by layer adsorption: gas molecules adsorb physically on the solid surface forming successive layers, in principle without a strict upper limit to the number of layers.
- Local interactions between adjacent layers: molecules interact significantly only with the layer directly above or below, rather than with distant layers.
- Langmuir behavior within each layer: the adsorption process in each layer can be treated analogously to Langmuir adsorption, while the first layer is distinguished by its stronger interaction with the solid surface compared with subsequent layers.

These hypotheses enable the derivation of an analytical relationship between the quantity adsorbed and the relative pressure, which can be exploited to determine the amount of adsorbate corresponding to monolayer capacity and, from that, the surface area. In practice, BET surface area measurements are most commonly performed using nitrogen (N_2)

adsorption at 77 K, at the boiling point of liquid nitrogen. At this temperature nitrogen is below its critical temperature, and physisorption is sufficiently strong to produce well defined adsorption isotherms. The experiment consists in measuring the adsorbed volume (or amount) of N_2 as a function of equilibrium pressure. By estimating the amount of nitrogen required to form a complete monolayer, and knowing the molecular cross sectional area of the adsorbate, the total accessible surface area of the sample (including the internal surface of accessible pores) can be deduced. Pores that are not accessible to the gas are, by definition, not detected by this method [82].

Physisorption isotherms are conventionally classified into six main types. In this context, BET analysis is considered most reliable for:

- Type II isotherms, typical of nonporous or macroporous solids where multilayer adsorption proceeds on an open surface;
- Type IV isotherms, characteristic of mesoporous materials (pore diameters approximately between 2 to 50 nm), where multilayer adsorption is followed by capillary condensation.

In the Figure 2.4, all the possible isotherm types are shown.

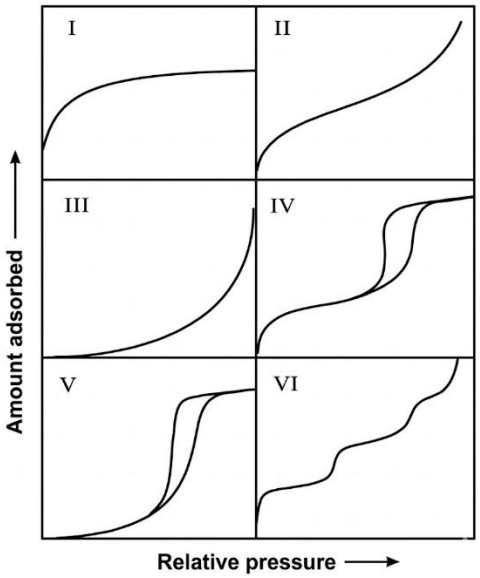

Figure 2.4. Types of adsorption isotherm.

Conversely, BET analysis is generally not reliable when the solid substantially absorbs the measuring gas or when the adsorption is dominated by phenomena that violate the model assumptions (e.g., strong specific interactions, pronounced microporosity effects, or chemisorption).

The BET is based on the following equation (Equation 2.1) [83] :

$$\frac{p}{n_a(p_0 - p)} S_{\text{total}} = \frac{1}{n_m C} + \frac{C - 1}{n_m C}\left(\frac{p}{p_0}\right) \qquad (2.1)$$

Where:

- p is the equilibrium pressure
- p_0 is the saturation vapour pressure of the adsorbate at the adsorption temperature,
- n_a is the adsorbed amount (often reported in moles)
- n_m is the monolayer capacity
- C is the BET constant
- S_{total} is the total surface area, function of n_m

The constant C is related to the energetic preference of adsorption in the first layer relative to subsequent layers and is therefore interpreted as an indicator of the strength of adsorbent–adsorbate interactions.

The BET plot is constructed by plotting $p/n_a(p_0 - p)$ versus p/p_0. A semi linear region is typically identified at relative pressures $p/p_0 \approx 0.05 - 0.35$, within which the BET model predicts an approximately straight line. The specific surface area is obtained by normalizing total surface area S_{total} by the sample mass.

In terms of experimental setup, BET Method operates the following phases [84]:

- Heat the sample and evacuate (or flush with N_2) to remove contaminants from the surface.
- Apply vacuum to the sample tubes to ensure a clean, controlled starting condition.
- Measure the tube's dead volume using He (helium doesn't adsorb significantly), so the instrument can correct gas-volume calculations.
- Re-evacuate after the He step to remove the helium and reset the system.
- Dose N_2 and record the adsorption isotherm (amount adsorbed vs relative pressure), where monolayer formation is used for BET surface area.
- Evacuate stepwise and record the desorption isotherm (gas released), often used together with adsorption to assess pore behavior and eventual hysteresis.

The apparatus used for BET measurements is showed in Figure 2.5

Figure 2.5. Apparatus used for BET.

2.2.2 Transmission Elettron Microscopy (TEM)

Transmission electron microscopy (TEM) is a technique able to characterize samples at an atomic level, achieving resolution in the order of the 1 nm, higher than light microscope. In catalyst context, this technique is extremely useful for delineating structure and composition on the nanoscale, which directly impact on properties of the material. [85]

Firstly introduced by the German engineer Max Knoll in 1931, TEM exploits the quantum behavior of electrons. The latter are emitted by an electron gun, normally consisting of a cathode made of tungsten or lanthanum hexaboride. Electrons emitted from the cathode are accelerated toward an anode under a precisely stabilized high voltage, producing a beam with a defined energy. The emission process is regulated by a control grid, known as Wehnelt cylinder, which ensures proper beam alignment and intensity. The focusing mechanism in TEM is based on the wave–particle duality of electrons: although electrons are negatively charged particles, they also exhibit wavelike behavior. As charged particles, they can be deflected and focused by magnetic or electric fields generated by electromagnetic lenses and metal apertures within the microscope column. This principle underlies not only electron microscopy but also technologies such as cathode-ray tubes and display devices.

Between the electron gun and the specimen, the condenser lens system controls the beam's intensity, convergence, and angular aperture. Often configured as a double condenser system, it allows adjustment of the illuminated area and enables the formation of nearly parallel electron beams when required. This configuration is particularly important for obtaining crystallographic information, as parallel illumination facilitates diffraction phenomena that reveal structural details of the specimen.

The specimen is mounted on a sample holder, commonly referred to as a TEM grid, which consists of a metal frame supporting a thin carbon-based film. The grid is positioned in the path of the electron beam using a mechanically controlled stage. For effective transmission, the specimen thickness typically must not exceed approximately 100 nm. The degree of electron transmission depends strongly on the material's thickness, density, and composition: porous or low-density materials allow more electrons to pass through, whereas denser regions scatter or absorb electrons more significantly, generating contrast in the final image.

After interacting with the specimen, the transmitted electrons carry information about its morphology, density distribution, and crystal structure. These electrons are then refocused by the objective lens, which produces a real intermediate image. The image is further magnified by an electromagnetic lens system composed of intermediate and projector lenses, enabling final magnifications typically ranging from 1,000X to 250,000X on the viewing screen. Image quality depends critically on precise mechanical alignment, electromagnetic lens stability, and highly stabilized power supplies, often requiring electronic control systems to maintain optimal resolution.

Finally, the electron image, intrinsically monochromatic, is converted into a visible form. The magnified electron beam is projected onto a phosphor (fluorescent) screen, where it is transformed into visible light, or captured digitally by a camera for display on a computer monitor. Digital images, stored in formats such as TIFF or JPEG, can be processed and analyzed using dedicated software. Post-acquisition processing, including contrast enhancement, may be applied to facilitate interpretation and scientific communication.

In order to increase the mean free path of electrons and minimize their interaction with gas molecules, a conventional transmission electron microscope (TEM) operates under high-vacuum conditions, typically at pressures on the order of 10^{-4} Pa. Such low pressures are required for two primary reasons.

First, the substantial potential difference applied between the cathode and ground, necessary to accelerate the electron beam, must be maintained without electrical discharge. A sufficiently high vacuum prevents arcing phenomena that could otherwise occur in the presence of residual gas.

Second, reducing the gas pressure significantly decreases the probability of collisions between electrons and gas atoms. These collisions would lead to energy loss, beam scattering, and a reduction in image resolution. By operating at very low pressures, the electron mean free path is greatly increased, ensuring that electrons travel through the microscope column with minimal interaction and preserving beam coherence and stability.

Because various components of the TEM must be periodically inserted, removed, or replaced, the system cannot be permanently sealed under vacuum. Consequently, TEM instruments are equipped with multiple pumping systems and airlock chambers that allow localized venting and rapid evacuation. This design ensures both operational flexibility and the maintenance of the stringent vacuum conditions required for optimal performance.[86]

Figure 2.6 shows a schematic representation of various components in a transmission electron microscope:

Figure 2.6. TEM schematic representation, modified from www.Britannica.com.

In the present dissertation, transmission electron microscopy (TEM) was employed to determine the mean particle size of Pt nanoparticles in two catalyst samples: Pt/CeO_2 LSA and Pt/CeO_2 MSA. Because TEM measurements are conducted under vacuum conditions

at (approximately) room temperature, require electron transparent specimens of adequate thickness, the catalysts were prepared as dilute dispersions prior to imaging. Specifically, two suspensions were obtained by dispersing each catalyst powder in isopropanol, followed by vortex mixing for 10 minutes to promote deagglomeration and ensure a homogeneous distribution of particles.

After mixing, an adequate quantity of the resulting suspensions were collected using a micropipette and deposited dropwise onto copper TEM grids. The grids consisted of a copper mesh ("lattice") coated with a thin carbon support film, which provides mechanical stability and an electron transparent background suitable for imaging. The deposited droplets were then allowed to dry, yielding a thin, well-dispersed catalyst layer appropriate for TEM observation and subsequent particle-size analysis.

During the observation, representative micrographs were acquired and subsequently processed using the ImageJ software package. Particle diameters were measured directly from the TEM images, and the resulting dataset was used to calculate the mean particle size for each Pt-sample.

2.2.3 X-ray diffraction

X-ray diffraction (XRD) is a central technique in materials characterization for probing the crystallographic structure of solids. By measuring the angles and intensities of X-rays diffracted by a periodic atomic lattice, XRD enables the identification of crystalline phases and the determination of key structural parameters such as lattice spacings, unit-cell symmetry, and preferred orientation (texture). Because the diffraction signal arises from long-range periodic order, XRD is particularly informative for crystalline and semi-crystalline materials.

The physical basis of XRD is the elastic interaction between an incident X-ray beam and the electron density surrounding atoms. X-rays have wavelengths on the order of interatomic distances (typically ~0.5–2 Å), which allows them to be diffracted by families of lattice planes in a crystal. When an X-ray beam impinges on a crystalline specimen, each set of parallel atomic planes can be treated as a periodic array of scatterers. The scattered waves propagate in many directions; however, only specific directions satisfy the geometric condition for constructive interference. In these directions, the scattered waves add coherently, producing intense diffraction maxima (peaks) that form the characteristic diffraction pattern of the material. In contrast, directions that do not satisfy the interference condition yield weak intensity due to partial or complete destructive interference.

In laboratory diffractometers, X-rays are commonly produced in an X-ray tube operating on principles analogous to a cathode-ray device. A heated filament (cathode) emits electrons via thermionic emission; these electrons are accelerated toward a metallic anode (the target) under a high potential difference. Upon striking the target, the energetic electrons can eject inner-shell electrons of the target atoms. Subsequent electronic transitions from higher-energy shells to fill these vacancies release photons in discrete energy lines, generating a characteristic X-ray spectrum superimposed on a continuous background. The most frequently used characteristic lines are the K-series, in particular K_α and K_β. The Kα emission itself is composed of closely spaced components (commonly denoted K_{α_1} and K_{α_2}), with K_{α_1} having slightly shorter wavelength and higher intensity than K_{α_2}; in routine diffraction practice, these two components are often treated through an effective, intensity-weighted average wavelength. The emitted wavelengths depend on the anode material (e.g., Cu, Fe, Mo, Cr), and copper is widely employed in laboratory XRD because its K_α radiation is well suited to many crystalline inorganic materials.

For diffraction measurements, the polychromatic output of the tube is conditioned to approximate monochromatic radiation. This is achieved by spectral filtering and/or by using crystal monochromators to select a narrow wavelength band. The resulting beam is then collimated and directed onto the specimen to ensure controlled beam divergence and reproducible diffraction geometry.

The relationship between diffraction angle and interplanar spacing is captured by Bragg's law, depicted in Equation 2.2, which provides the fundamental link between measured peak positions and crystal structure [87] :

$$n\lambda = 2d \sin\theta \qquad (2.2)$$

Where:

- n is an integer, namely the diffraction order
- λ is the X-ray wavelength

- d is the spacing between the relevant set of lattice planes
- θ is the Bragg angle (half of the commonly reported scattering angle 2θin standard diffractometer geometries).

Conceptually, Bragg's law is obtained by requiring that the path-length difference between waves scattered from successive planes equals an integer multiple of the wavelength. When this condition is satisfied, constructive interference produces a measurable increase in diffracted intensity, observed as a peak in the recorded pattern. The experimental concept behind XRD and De Broglie concept of diffraction are well depicted in Figure 2.7;

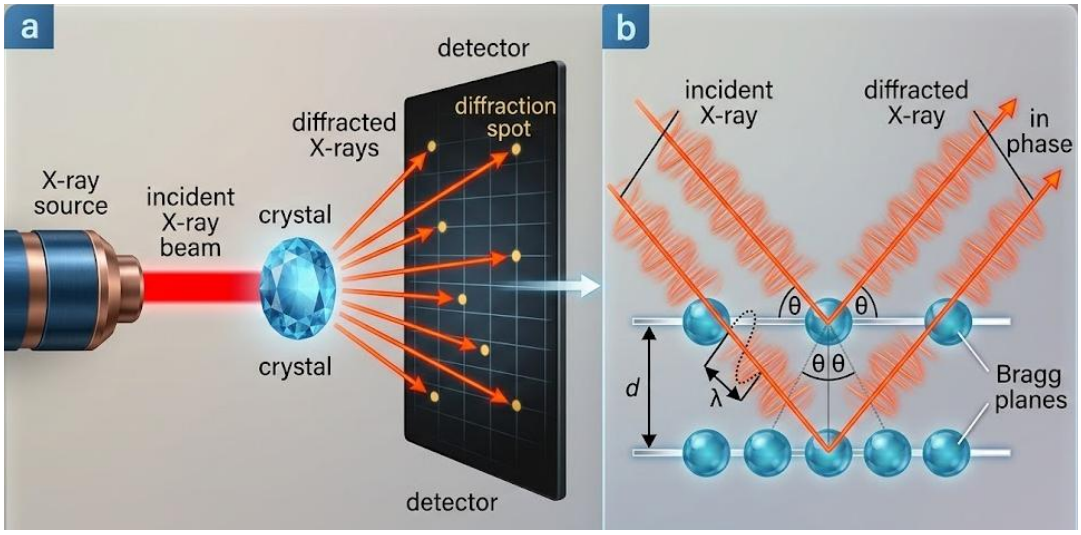

Figure 2.7. XRD experiment (a) and De Broglie diffraction (b), modified from [88]

From an instrumental perspective, most powder diffractometers adopt a θ–2θ geometry. The sample is positioned in the path of the incident, collimated beam and is rotated by an angle θ, while the detector is mounted on a rotating arm that moves through an angle 2θ to collect the diffracted radiation. The mechanical assembly that precisely controls these coupled angular motions is the goniometer, which ensures accurate alignment and reproducibility of the diffraction angles. During a scan, the detector converts the incoming X-ray signal into an electronic output proportional to intensity; this signal is processed and reported as a count rate as a function of 2θ, typically displayed and stored digitally for subsequent analysis.

In practical laboratory measurements, XRD is most often performed using a powder diffractometer in a θ–2θ configuration, where the sample and detector rotate such that the detector records intensity as a function of 2θ. For polycrystalline (powder) materials, the specimen contains a large number of randomly oriented crystallites. This statistical distribution ensures that, for each family of lattice planes, some crystallites satisfy the Bragg condition at a given angle, producing peaks at reproducible 2θ positions. Beyond phase identification, peak shapes and widths can provide microstructural information: peak broadening is commonly associated with small crystallite size and/or lattice strain, and variations in relative peak intensities can indicate texture or preferred orientation. When crystallites are very small (e.g., nanocrystalline materials) or when crystallinity is limited, the diffraction peaks may broaden substantially and the pattern may include a significant diffuse background; even in these cases, XRD remains valuable for assessing crystallinity, estimating average crystallite size (with appropriate models), and evaluating phase purity.

In the analysis, the measured 2θ values are used to determine d-spacings through Equation 2.2 and to calculate the lattice parameter a. Because systematic experimental effects (e.g., specimen displacement, transparency, and instrumental aberrations) can cause small peak-position errors, especially at low and intermediate angles, an established refinement approach is the Nelson–Riley extrapolation [89]. In this method, for each reflection one computes an apparent lattice parameter $a(\theta)$ and plots it as a function of the Nelson–Riley function, showed in Equation 2.3:

$$f(\theta) = \left(\frac{\cos^2\theta}{\sin\theta}\right) + \left(\frac{\cos^2\theta}{\theta}\right) \tag{2.3}$$

then extrapolates the trend toward $f(\theta) \to 0$ (high-angle limit) to obtain a more accurate estimate of the true lattice parameter by minimizing angular-dependent systematic errors.

Beyond peak positions, the breadth of diffraction peaks contains microstructural information. In particular, finite crystallite dimensions lead to line broadening, and the average size of coherently diffracting domains can be estimated using the Scherrer equation, showed in Equation 2.4:

$$C_s = \frac{K\lambda}{\beta\cos\theta} \tag{2.4}$$

Where :

- C_s is the average crystallite size,
- K is a dimensionless shape factor, commonly ~ 0.9 for approximately spherical domains
- λ is the X-ray wavelength,
- β is the full width at half maximum (FWHM) of the reflection expressed in radians
- θ is the Bragg angle.

The Scherrer approach is widely applied in powder diffraction to obtain a first-order estimate of nanocrystalline or sub-micrometric domain sizes.

In the present dissertation, X-ray diffraction (XRD) analysis was performed on all samples (Pt/CeO_2) and supports (CeO_2) using Cu Kα radiation with a wavelength (λ) of 1.5418 Å. The diffraction patterns were recorded over a 2θ range from 20° to 80°, employing a step size of 0.0131° and a counting time of 88.9 s per step.

2.2.4 Hydrogen temperature-programmed reduction

Hydrogen temperature-programmed reduction (H_2-TPR) is a widely used technique for the physicochemical characterization of heterogeneous catalysts, particularly those containing reducible metal oxides. Its primary purpose is to evaluate reducibility, that is the tendency of oxidized species to be reduced under hydrogen, as well as to infer oxidation states, the distribution/dispersion of oxide phases, and the strength of metal–support interactions. Because the reduction of distinct surface and bulk species occurs at different temperatures, the resulting signal typically provides a characteristic "fingerprint" that can be compared across samples to assess changes in composition, morphology, or interaction with the support. [90]

At its core, H_2-TPR monitors hydrogen uptake while the catalyst is subjected to a controlled, linear temperature ramp under a dilute hydrogen stream. The generalized reduction reaction for a metal oxide (MO_x) can be expressed as:

$$MO_x + xH_2 \rightarrow M + xH_2O$$

where the exact stoichiometry and final reduced state depend on the metal, its initial oxidation state, and the experimental conditions. As temperature increases, successive reduction steps may occur (for example, higher oxidation states reducing first to intermediate oxides and then to the metallic state), generating multiple features in the recorded profile.

In a typical H_2-TPR setup, the sample is placed in a fixed-bed reactor (often a quartz U-tube) and exposed to a flowing mixture of hydrogen diluted in an inert carrier gas such as argon or nitrogen. Dilution is used to maintain stable operation and to ensure that hydrogen consumption remains within the detection range. The temperature then is increased at a constant heating rate, while the outlet gas composition is continuously analyzed.

Hydrogen consumption is commonly measured using a thermal conductivity detector (TCD). The TCD responds to changes in the thermal conductivity of the gas stream: when hydrogen is consumed during reduction, its concentration decreases in the effluent, altering the thermal conductivity relative to a reference flow. The detector output is plotted as a function of temperature, yielding the TPR profile. In this profile, each peak corresponds to a reduction event, and the peak temperature (or temperature range) reflects the kinetic and thermodynamic accessibility of that reduction step.

Reliable TPR measurements depend strongly on appropriate sample pre-treatment and on controlling secondary effects that may distort the detector signal. Prior to analysis, catalysts are typically dried and conditioned to remove physiosorbed water and other weakly bound contaminants that could contribute spurious signals or alter reduction behavior. During reduction, water is produced as a reaction product; if not removed, it can interfere with the detector response and may also participate in re-adsorption or hydroxylation phenomena. For this reason, the effluent is often passed through a cold trap to condense water before the gas reaches the TCD, improving baseline stability and protecting detector performance.

The analytical value of H_2-TPR lies in how peak position, shape, and integrated area relate to catalyst properties:

- Peak temperature: Lower reduction temperatures generally indicate more readily reducible species (e.g., highly dispersed surface oxides or weakly interacting phases), whereas higher temperatures can indicate bulk-like oxides, strongly bound species, or phases stabilized by the support.

- Multiple peaks: The presence of several peaks is often interpreted as evidence of multiple reducible species and/or multiple oxidation states undergoing sequential reduction steps. This is particularly relevant for mixed oxides and supported systems where surface and bulk domains may reduce differently.
- Peak area (quantification): Integrating the peak area provides the total hydrogen consumed during the corresponding reduction event. With proper calibration, this can be converted into moles of H_2, enabling quantitative assignment to specific oxidation state changes and allowing estimation of the fraction of a phase that is reducible under the applied conditions. The calibration procedure enables the determination of the calibration factor, C_F. This factor is obtained by introducing a 5% H_2/N_2 gas mixture over around 20 mg of cupric oxide in the TPR apparatus, promoting the complete reduction of the oxide. Since the total amount of reducible copper species is known, the corresponding integrated signal area can be used to calculate C_F. This calibration factor subsequently allows each integrated peak area recorded during TPR analysis to be quantitatively correlated with a specific amount of hydrogen consumed.

It is important to note that peak shapes and apparent reduction temperatures can also be influenced by transport phenomena, heating rate, particle morphology, and dispersion. In this context, modeling approaches that account for features such as particle-size distributions can help rationalize peak broadening or multi-step behavior, and they are particularly useful when comparing catalysts with different degrees of dispersion or heterogeneous oxide domains (e.g., work discussing particle-size distribution effects in metal oxide TPR) [91].

In Figure 2.8, it is reported the apparatus used in this dissertation for the TPR analysis:

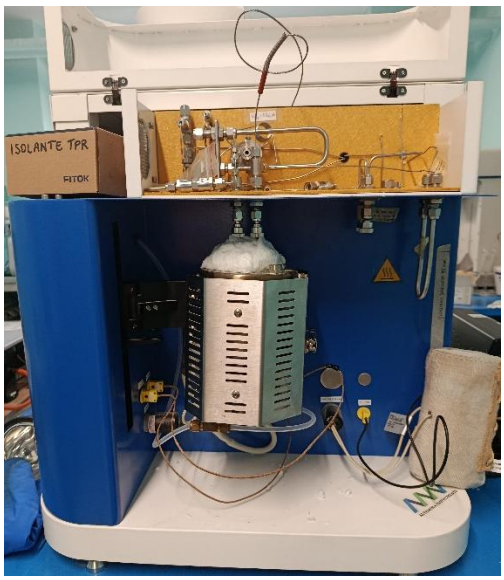

Figure 2.8. H_2 TPR reactor.

In this dissertation, H_2 TPR was conducted on all the samples synthetized, both platinum based and supports (Pt/CeO_2 and CeO_2). For each sample, approximately 50 mg of material was weighed and packed into the reactor between two plugs of quartz wool. The reactor, a U-shaped quartz tube, was then positioned inside a tubular furnace.

An initial pretreatment was performed by flowing helium at 25 mL/min while heating the sample to 550 °C at a rate of 5 °C/min. The temperature was held at 550 °C for 1 h and subsequently decreased to 100 °C at 10 °C/min.

A second pretreatment step followed, aimed at saturating surface acid sites. To this end, a 5% H_2/N_2 mixture was introduced at 40 mL/min at 100 °C for 30 min.

Physically adsorbed ammonia was then removed by purging with helium at 40 mL/min for 30 min. The desorption stage was carried out by heating the reactor to 600 °C at 10 °C/min under nitrogen (carrier gas) flowing at 25 mL/min. The final temperature was maintained for 30 min, after which the system was flushed with helium at 35 mL/min for 1 min.

At the end of the measurement, during the cooling phase, a pulse calibration was performed. Helium was continuously supplied at 25 mL/min (the same flow rate used during analysis), and periodic pulses of 524 μL of a 5% H_2/N_2 mixture were injected into the stream. A total of 10 pulses were applied, with data acquisition set to one point every 0.3 s

2.2.5 Carbon monoxide Chemisorption (CO Chemisorption)

Carbon monoxide (CO) chemisorption is an analytical technique extensively utilized for the morphological and chemical characterization of supported metal catalysts. Operating primarily through either static volumetric or dynamic pulse methodologies. It is particularly efficacious for characterizing Group VIII transition metals, including Pt, where the catalytic activity is intrinsically linked to the availability of active surface sites. The accuracy of CO chemisorption relies on treatments to ensure that only the active metal surface interacts with the adsorbate.

In the CO chemisorption analysis, indeed, the catalyst is first subjected to thermal drying to eliminate physiosorbed moisture. Subsequently, it undergoes a temperature-programmed reduction (TPR), typically utilizing hydrogen gas (H_2) at elevated temperatures. This crucial step reduces the precursor metal oxides to their zero-valent, metallic state.

Following reduction, the system is purged with an inert carrier gas (such as Helium or Argon) while maintaining or modifying the elevated temperature. This facilitates the complete desorption of residual hydrogen from the metal lattice and surface, preventing competitive adsorption during the subsequent dosing phase. Once the sample is cooled to an ambient temperature, CO is introduced. This can be executed through reproducible loop injections (pulse method). The objective is to achieve a saturated chemisorbed monolayer of CO on the metal surface. In the dynamic pulse method, a Thermal Conductivity Detector (TCD) continually monitors the effluent gas stream. The TCD measures the concentration of unadsorbed CO following each pulse. Complete peak area integration of allows for the precise calculation of the total volume of CO consumed by the sample. [92]

The fundamental purpose of CO chemisorption is to empirically determine intrinsic catalytic properties that govern reaction kinetics and overall catalytic efficiency. The analysis leads to critical parameters:

- metal dispersion, that is defined as the ratio of moles of Platinum to moles of CO adsorbed. High dispersion is indicative of optimized metal utilization, which is crucial for minimizing the cost of precious metal catalysts
- average crystallite size, derived from the dispersion and surface area calculations under the assumption of a specific crystallite geometry, generally hemispherical).

A key parameter in chemisorption calculations is the stoichiometric factor, which is the ratio of adsorbed CO molecules to exposed surface metal atoms. Because CO binding depends on σ-donation and π-backdonation with metal *d* orbitals, different adsorption modes are possible. Among these, the most relevant are linear, bridge and twin adsorption. In the linear type, one CO molecule binds to a single surface metal atom ($\mathrm{CO:M} = 1:1$). In the bridge adsorption, CO molecule coordinates across two adjacent surface metal atoms ($\mathrm{CO:M} = 1:2$). Finally, in the twin (geminal) adsorption CO molecules coordinate to a single metal atom or ion ($\mathrm{CO:M} = 2:1$). For Platinum, many studies have underlined how CO adsorption takes place in a linearly bound configuration on the metal surface. [93], [94]

In the present dissertation, the CO chemisorption was conducted on all the samples containing platinum:

- Pt/CeO_2 LSA
- Pt/CeO_2 MSA
- Pt/CeO_2 HSA

More specifically, for each sample, approximately 50 mg of powder was weighed and loaded into the reactor between two plugs of quartz wool. The reactor, consisting of a U-shaped quartz tube, was placed inside a furnace, the same used even for H_2 TPR. The samples first underwent an initial pretreatment consisting of inertization with argon (30 mL/min) at 50 °C for 5 min to remove residual air. This was followed by a reduction step in which a gas mixture containing 5% H_2 in Ar was introduced while heating the samples to 300 °C at a rate of 10 °C/min. The final temperature was maintained for 60 min to reduce platinum to its metallic state.

After removing hydrogen by purging with helium (30 mL/min) for 20 min at 300 °C, CO chemisorption measurements were performed at 30 °C. Helium was continuously supplied as the carrier gas (25 mL/min), owing to its high thermal conductivity and its strong contrast with CO. Within this stream, 524 µL pulses of a mixture containing 10% CO in He were injected every 4 min. The outlet gas composition was monitored using a TCD. Ten pulses were applied, and data were recorded at a sampling interval of 0.3 s. Following a brief helium purge (30 mL/min) for 1 min, the TCD was calibrated using five pulses under conditions comparable to those of the analysis; however, the gas was directed through a bypass (null station) rather than the reactor to prevent chemisorption on the catalyst.

From the data obtained during the experimental procedure, and by integrating the differences between successive pulses, the metal dispersion (d_{is}) was calculated according to Equation 2.5 [95]:

$$d_{is} = \frac{n_{\mathrm{mol}} \cdot p}{MW_{Pt} \cdot W \cdot f} \qquad (2.4)$$

where:

- n_{mol} represents the number of moles of CO, determined using the Ideal Gas Law;
- p denotes the ratio between the mean integrated pulse area and the missing area;
- MW_{Pt} is the atomic weight of the active metal;
- W corresponds to the total mass of the catalyst sample;

- f indicates the mass fraction of the active metal in the catalyst (in this case, 0.005, corresponding to a 0.5 wt.% metal loading).

It should be noted that the stoichiometric factor was not included in the calculation, as it is equal to unity for linearly adsorbed CO.

The parameter $p$is determined by considering that the pulses recorded by the TCD exhibit different peak heights and, consequently, different integrated areas, as it is clearly shown in Figure 2.9. A decrease in the pulse area corresponds to a greater amount of CO adsorbed during the analysis, as less CO remains in the gas phase to be detected.

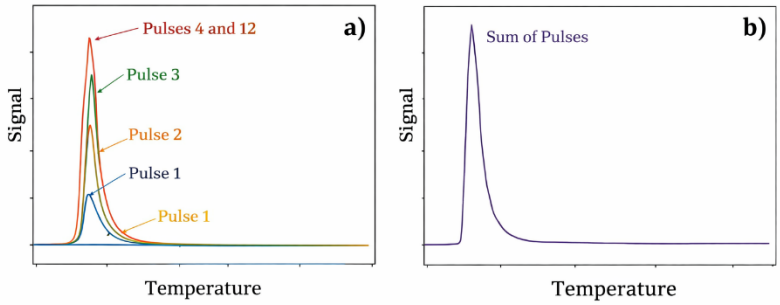

Figure 2.9. Sequence of pulses in a Pt-based catalyst, to arrive at complete saturation, modified from www.ami-instruments.com.

Assuming the spherical form of Platinum nanoparticles, it is possible to calculate the equivalent hemispherical diameter D, according to Equation 2.5 [96]:

$$D = \frac{6}{\rho_{Pt}\, d_{is}\, N_A\, \sigma_{Pt}} \tag{2.5}$$

where:

- ρ_{Pt} represents the density of Platinum;
- d_{is} denotes the Platinum dispersion;
- N_A is the Avogadro number;
- σ_{Pt} is the cross-sectional area for each Platinum atom.

D is an equivalent average particle size derived from chemisorption data under the assumption of hemispherical particle geometry, rather than as a direct measurement of the actual nanoparticle diameter.

2.3 Catalytic tests

Catalytic tests were conducted using a custom-built experimental reactor system, referred to as “Dragon” The setup consists of an electrically heated furnace equipped with a PID temperature controller to ensure accurate and stable thermal regulation. Temperature was continuously monitored by means of a type K thermocouple positioned in close proximity to the catalytic bed, allowing precise control of the reaction conditions. Insulation from external environment was ensured from quartz wool. The system includes dedicated reactor lines as well as a bypass line, enabling stabilization of the gas mixture prior to contact with the catalyst and facilitating reliable baseline measurements. The reactant gas streams were delivered through a valve manifold and regulated by mass flow controllers operating under PID control. The setup used is shown in Figure 2.10.

Figure 2.10. Dragon Apparatus.

Two types of catalytic test were performed, to assess both activity and durability of the investigated materials :

- Conversion tests carried out to determine the catalytic performance as a function of temperature. In these experiments, the conversion of selected target species, carbon monoxide and ethylene, was monitored while progressively increasing the reaction temperature from ambient conditions to higher values. This temperature-programmed approach enabled the identification of key performance parameters, including light-off behavior and the temperature required to achieve complete conversion. The resulting conversion-temperature profiles provided a comparative assessment of catalytic activity among the different samples.
- Stability tests (Time on Stream, TOS) were conducted to evaluate both the thermal robustness and the long-term performance stability of the catalysts under determinate reaction conditions. For each sample, a reaction temperature was selected to ensure a conversion level of at least 75–80%, thereby maintaining catalytically relevant operating conditions. The catalysts were then operated continuously for a duration of 24 hours. This extended testing period allowed for the detection of possible deactivation phenomena, structural or compositional changes, and fluctuations in catalytic efficiency over time, thus providing a more comprehensive assessment of catalyst durability.

All tests were performed under controlled and reproducible conditions using a U-shaped quartz reactor with an internal diameter of 4 mm. The reactor was packed with quartz wool as an inert support and loaded with approximately 50 mg of catalyst powder.

Pre-treatment procedures were adapted according to the type of catalyst investigated. For both the supports (CeO_2 LSA, CeO_2 MSA, CeO_2 HSA) and the Pt-based samples (Pt/CeO_2 LSA, Pt/CeO_2 MSA, Pt/CeO_2 HSA), an initial pre-treatment step was carried out to remove adsorbed contaminants and moisture, thereby preventing water from entering the analytical system. This step consisted of flowing 50 mL/min of air (21% O_2 and 79% N_2, molar basis) through the reactor while heating to 110 °C, followed by an isothermal hold at this temperature for 30 minutes.

In the case of the Pt-containing samples (Pt/CeO_2 LSA, Pt/CeO_2 MSA, Pt/CeO_2 HSA), an additional reduction step was performed to convert platinum species to their reduced state and enhance their catalytic oxidation activity. The reduction treatment was conducted under a flow of 50 mL/ min of a gas mixture containing 5% H_2 in 95% N_2 at 300 °C for 60 minutes.

After all pre-treatment steps, the reactor was allowed to cool to the room temperature prior to initiating the catalytic performance tests. As already mentioned, the catalytic tests were conducted on two main compounds, Carbon monoxide (CO) and Ethylene (C_2H_4).

In both cases, a mixture of 100 ppm of the target compounds was prepared, sending to the reactor a mole flow 50 mL/ min constituted by:

- 10.5 mL/min of O_2, 2.5 ml/min of CO/N_2 and 37 mL/min of N_2 for CO tests
- 8.5 mL/min of O_2, 5 ml/min of C_2H_4/N_2 and 34.5 mL/min of N_2 for C_2H_4 tests

2.3.1 Catalyst Performance evaluation

For assess the performance of the catalysts, fundamental parameters where evaluated, as conversion and turnover frequency (TOF).

Conversion is a well-known parameter used for quantify the target reactant transformed into product in a chemical reaction. In the case of CO oxidation, conversion X_{CO} was calculated according to Equation 2.5 [97] :

$$X_{CO} = \frac{[CO]_{in} - [CO]_{out}}{[CO]_{in}} \tag{2.5}$$

Where

- $[CO]_{in}$ is the concentration in ppm of CO in the inlet stream
- $[CO]_{in}$ is the concentration in ppm of CO in the outlet stream

In the case of ethylene, since the analyzer is not able to detect it, the conversion was referred to the detected CO2, the main product of reaction in C_2H_4 oxidation. The formula used is reported in Equation 2.6 :

$$X_{C_2H_4} = \frac{[CO_2]_{in} - [CO_2]_{out}}{[CO_2]_{in}} \tag{2.6}$$

The TOF is an indication of the quantity of product referred to active sites present, reflecting the intrinsic activity of catalysts. It is a meaningful indicator for comparing the catalytic activity of similar types of catalyst. Its general formula is provided by Equation 2.7 [98]:

$$\mathrm{TOF} = \frac{n_{prod}}{n_{cat} \cdot t} \tag{2.7}$$

Where:

- n_{prod} are the moles converted by the catalyst
- n_{cat} are the moles of catalyst
- t is the unit of time

3. Results and discussion

In this section, the experimental results are presented and critically discussed, with the aim of interpreting both the physicochemical characterization and the catalytic performance data. The discussion first focuses on the characterization of the catalysts, progressing from textural properties obtained by BET measurements to surface-metal quantification derived from CO chemisorption. Subsequently, the outcomes of the catalytic tests are examined, focusing on both reactant conversion and catalyst stability as a function of time on stream (TOS).

3.1 Characterization results

3.1.1 BET results

BET analysis was performed on all the samples, including the ones containing Platinum (Pt/CeO2 LSA, Pt/CeO2 MSA, Pt/CeO2 HSA) and the supports (CeO2 LSA, CeO2 MSA, CeO2 HSA). From this analysis, three principal textural properties were determined: specific surface area, pore volume, and pore size, reported in Table 3.1. Furthermore, the nature of the porosity was examined by analyzing the adsorption–desorption isotherms, which offered additional information on the pore structure and allowed the porous characteristics of the samples to be classified.

Sample	Surface Area (m^2/g)	Pore Volume (cm^3/g)	Pore Size (Å)
CeO_2 LSA	2.1	0.0062	37.6
CeO_2 MSA	59.5	0.098	43.4
CeO_2 HSA	122.6	0.22	61.2
Pt/CeO_2 LSA	1.9	0.006	37.6
Pt/CeO_2 MSA	58.8	0.095	42.3
Pt/CeO_2 HSA	125	0.20	60.8

For CeO_2 LSA and Pt/CeO_2 LSA samples, the calcination at 900°C induces significant thermal sintering and structural coarsening, leading to crystallite growth, pore shrinkage, and partial collapse of the mesoporous network. These effects reduce both the external and internal surface area, thereby explaining the marked decrease in specific surface area in respect to other samples. The same mechanism explains even the minor pore volume and pore size. [99]

CeO_2 MSA and Pt/CeO_2 MSA do not exhibit a reduced surface area, since final calcination was not conducted on these samples. The absence of this additional thermal treatment prevented extensive sintering and structural densification, thereby preserving the main textural characteristics of the materials. Consequently, both samples display values of specific surface area, pore volume, and pore size that are in accordance with those typically reported in the literature for ceria prepared via solution combustion synthesis (SCS). [100]

For CeO_2 HSA and Pt/CeO_2 HSA, it appears clear how the initial aim of using SBA-15 as templates for CeO_2 led to satisfying results. In fact, the templating action of SBA-15 promoted the development of a more structured porous framework, limiting particle agglomeration and favoring the formation of a ceria support with improved textural properties compared with conventionally prepared samples, in terms of surface area, but also of pore volume, and pore size.

The BET isotherms are reported in Figure 3.1 and Figure 3.2, for platinum based samples and supports, respectively.

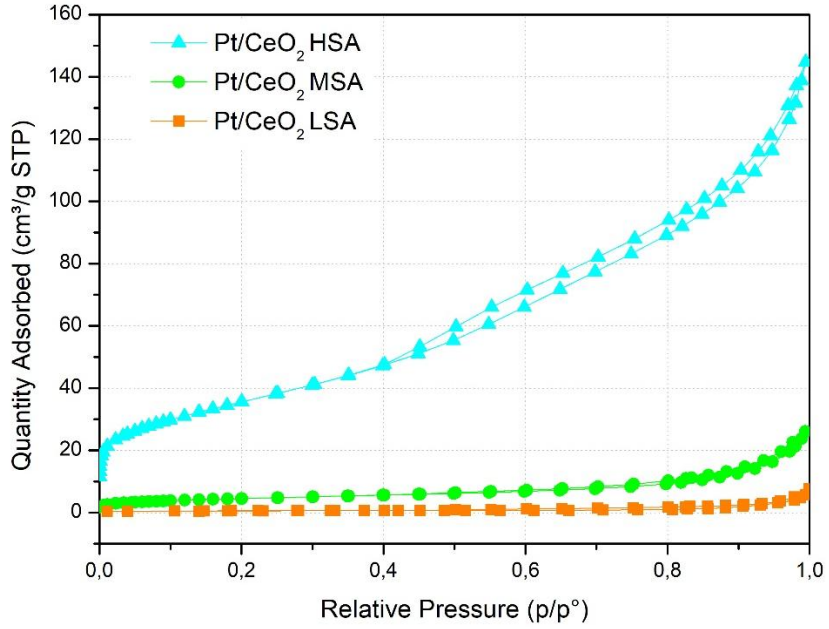

Figure 3.1. BET isotherm of adsorption-desorption for Pt/CeO_2 samples.

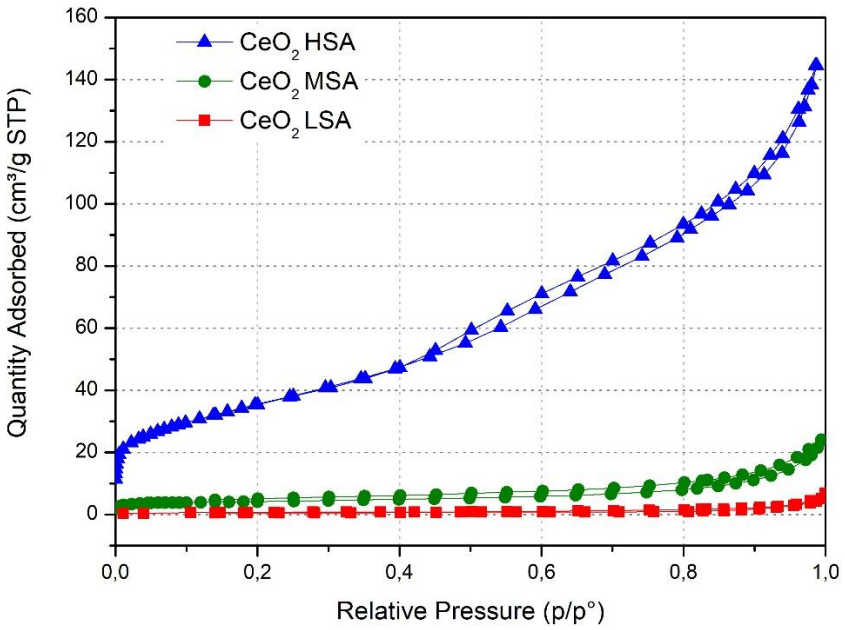

Figure 11. BET isotherm of adsorption-desorption for CeO_2 samples.

The adsorption-desorption isotherms exhibited previously can be classified as Type II according to the BET classification, which is typically associated with non-porous or macroporous solids. However, it is important to note that both Pt/CeO_2 HSA and CeO_2 HSA also exhibit a distinct hysteresis loop in the desorption branch and a moderate amount of N_2 adsorbed for low pressures. These features are generally indicative of the presence of mesoporosity, suggesting that, despite the overall Type II character of the isotherms, these samples possess a textural structure that includes mesoporous domains. [101]

3.1.2 TEM Analysis

As already mentioned in the previous section, TEM analysis was conducted on two platinum containing samples (Pt/CeO_2 LSA Pt/CeO_2 MSA) and also nanoparticles solution. The acquisitions on Pt/CeO_2 LSA Pt/CeO_2 MSA are reported respectively in Figure 3.3 (a) and 3.3(b).

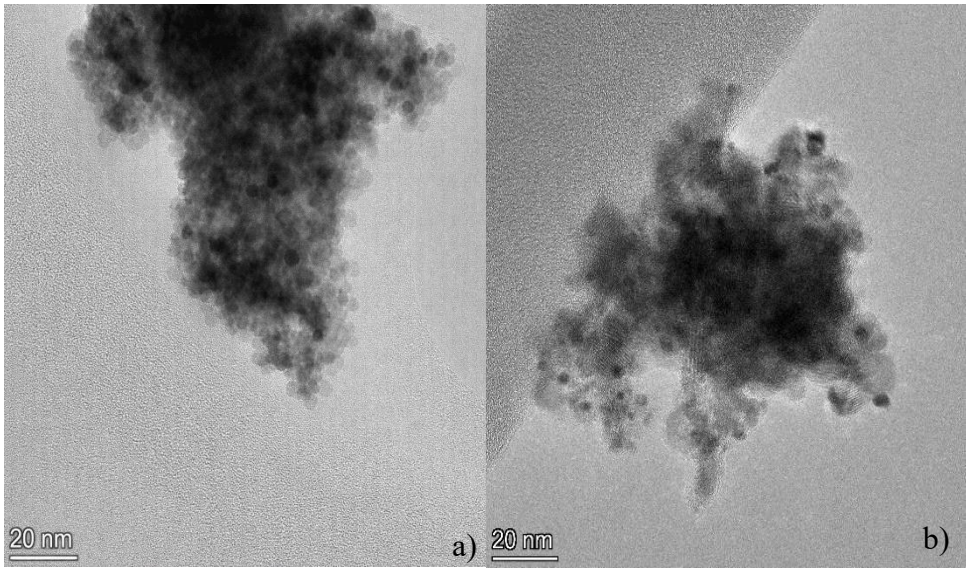

Figure 12. TEM images of Pt/CeO_2 LSA (a) and Pt/CeO_2 MSA (b).

As it is clear, the TEM acquisitions of Pt-based samples do not permit to obtain direct evidence of the presence and spatial distribution of platinum nanoparticles on the ceria support, preventing a qualitative comparison between the two samples in terms of particle dispersion and structural characteristics. For this reason, TEM analysis was conducted on nanoparticle solution, obtaining the acquisitions depicted in Figure 3.4. In Figure 3.4 (a) two representative nanoparticles are focused in detail in order to evaluate the diameter, respectively of 1.83 and 1.84 nm.

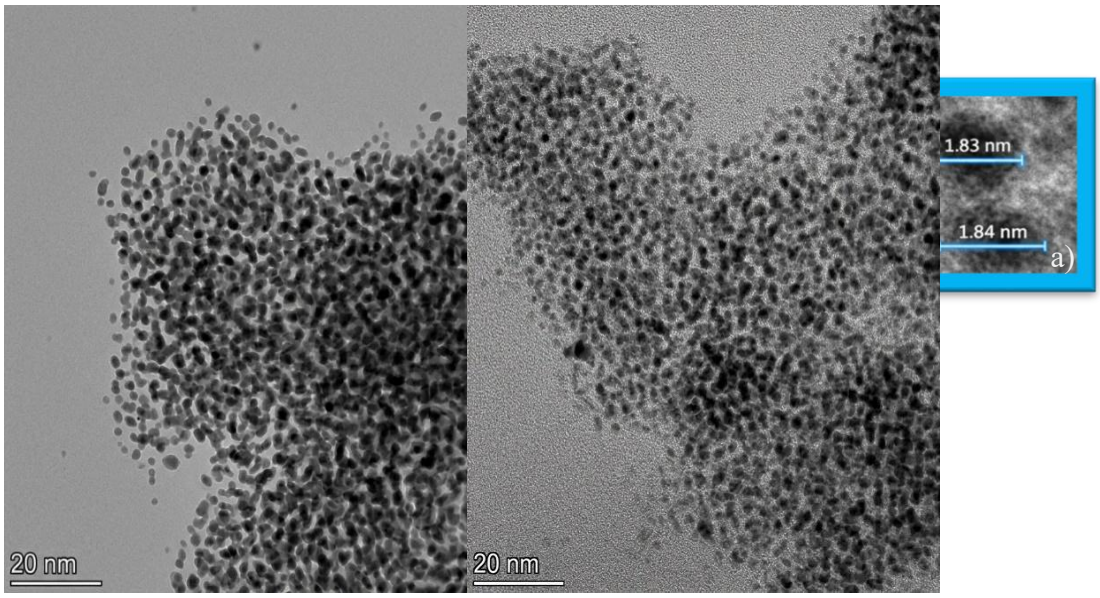

Figure 13. TEM micrographs of the platinum nanoparticle suspension, together with a magnified view of two representative nanoparticles (a).

By analyzing the TEM micrographs using ImageJ software, proper amount of platinum nanoparticles were individually selected and their diameters measured. The resulting diameter values were then compiled into a dataset, and the corresponding number-based particle size distribution is reported in Figure 3.5.

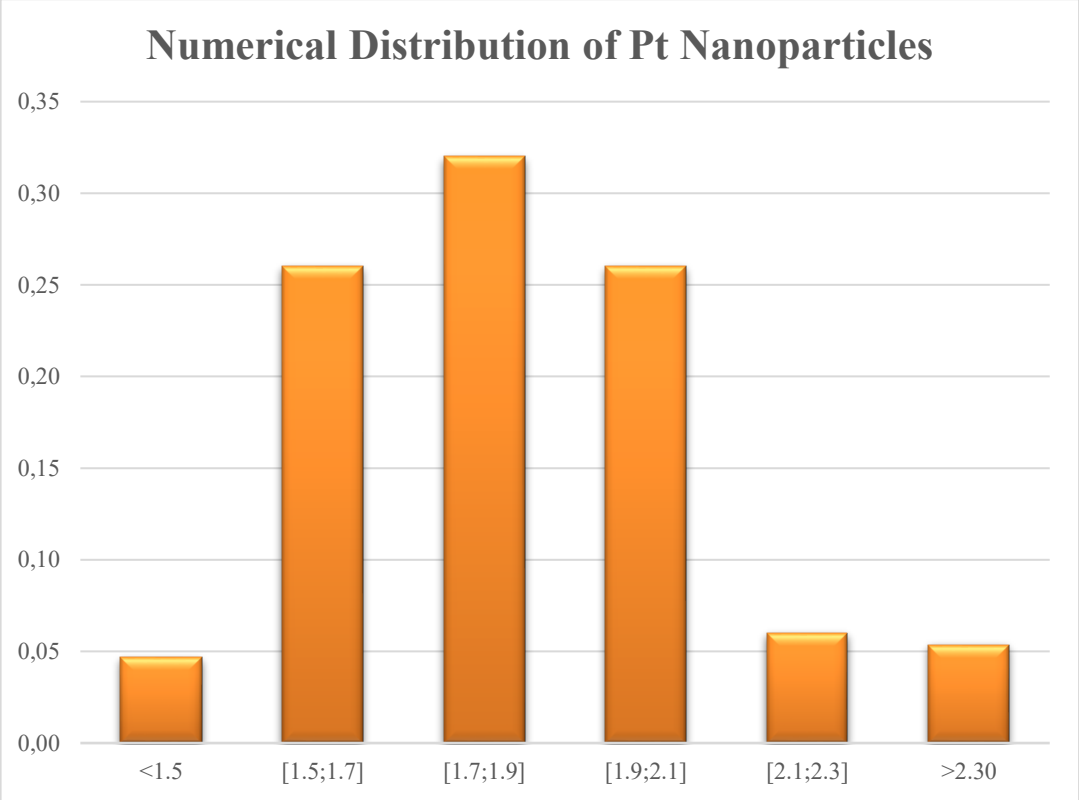

Figure 314 Number based particle size distribution of Platinum Nanoparticles.

The majority of the particles exhibit diameters in the range 1.5–2.10 nm, which is fully consistent with the objective of producing nanoscale platinum nanoparticles. Particle sizes in this interval are expected to promote an adequate metal dispersion on the support, increasing the number of accessible surface sites and supporting an effective utilization of the active phase.

For completeness, relevant statistic parameters were calculated: mean diameter, median, geometric mean were calculated. The results are reported in Table 3.1.

Table 3.1 Relevant mean statistic values

Mean Diameter (nm) =	1.83
Median Diameter (nm) =	1.82
Geometric Mean diameter (nm) =	1.81

After verifying the normality assumption for the dataset by means of a Q-Q plot, the expected value (Mean Diameter) μ and variance σ^2 were calculated. On the basis of these

parameters, the corresponding normal probability density function was derived and is shown in Figure 3.6.

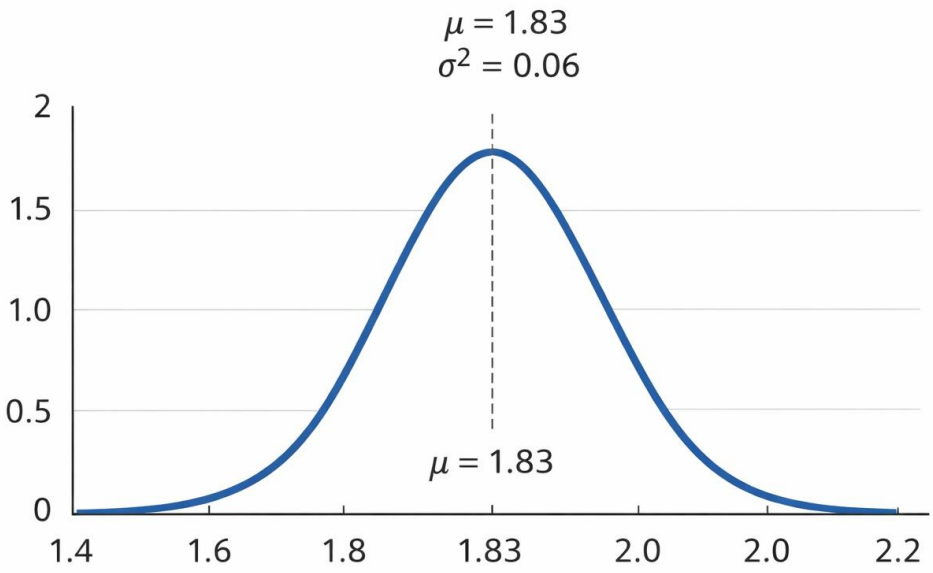

Figure 15 Normal probability density function associated with Pt particle size

3.1.3 XRD results

XRD analysis was carried out on all synthesized samples, including the Platinum based ones (Pt/CeO_2 LSA, Pt/CeO_2 MSA, Pt/CeO_2 HSA) and the supports (CeO_2 LSA, CeO_2 MSA, CeO_2 HSA), in order to investigate their crystalline structure and phase composition. For all samples, the diffraction patterns exhibited the characteristic reflections of fluorite-type CeO_2 with Bragg peaks associated to the crystallographic planes (111), (200), (220), (311), (222), (400), (331), and (420), as reported in Figure 3.7. These reflections are consistent with data commonly reported in scientific literature. [102]

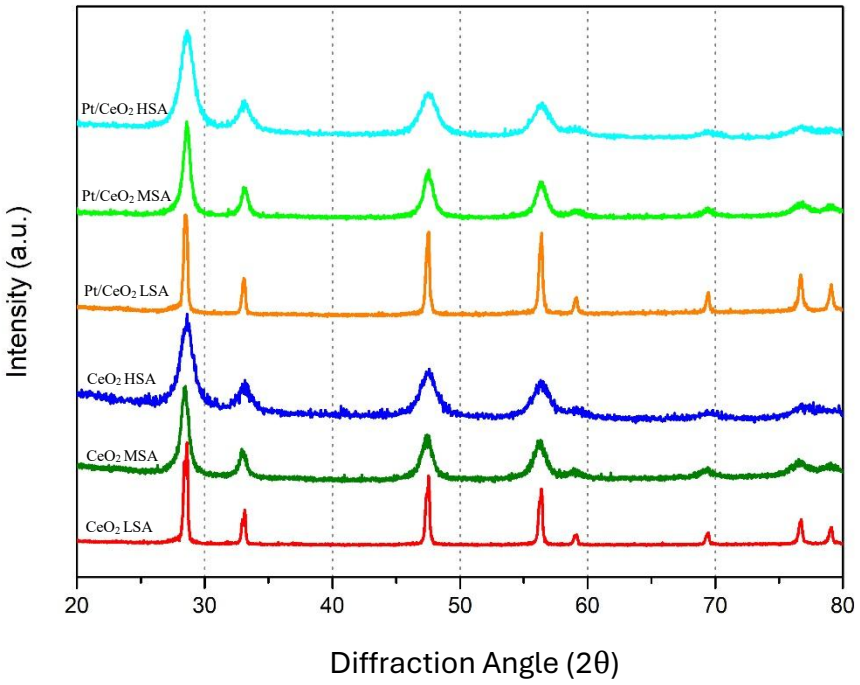

Figure 3.7. XRD patterns associated to all the synthesized samples.

No additional diffraction peaks attributable to secondary crystalline phases were observed in any of the analyzed samples in the investigated range (from $2\theta = 20°$ to $2\theta = 80°$), indicating that the adopted synthesis procedure did not lead to the formation of detectable impurities or by-products. In particular, in the platinum-containing samples, no reflections associated with metallic platinum were detected. More specifically, the characteristic Pt peaks generally assigned to the (111) and (200) planes, expected at approximately $2\theta = 39.8°$ and 46.2°, respectively, were absent from the diffractograms. [103]

This result can be reasonably attributed to the low platinum loading, equal to 0.5 wt.%, which may fall below the detection limit of the XRD technique. In addition, the absence of Pt-related reflections may also suggest that platinum is highly dispersed over the ceria surface and/or present in the form of very small crystallites, whose dimensions are insufficient to generate detectable diffraction peaks.

It is worth noting that, for Pt/CeO_2 HSA and CeO_2 HSA, the samples synthetized using SBA-15 as template, a diffraction peak located in the low-angle region, in proximity to $2\theta = 1°$, and associable to the (100) crystallographic plane of SBA-15 [101], was observed, as shown in Figure 3.8. The presence of this reflection strongly suggests that part of the

SBA-15 template remained within the samples after synthesis. This evidence indicates that the washing step was not fully effective in completely removing the silica template from the catalyst matrix. Consequently, residual SBA-15 may contribute to the structural features detected in the XRD pattern, particularly in the low angle region.

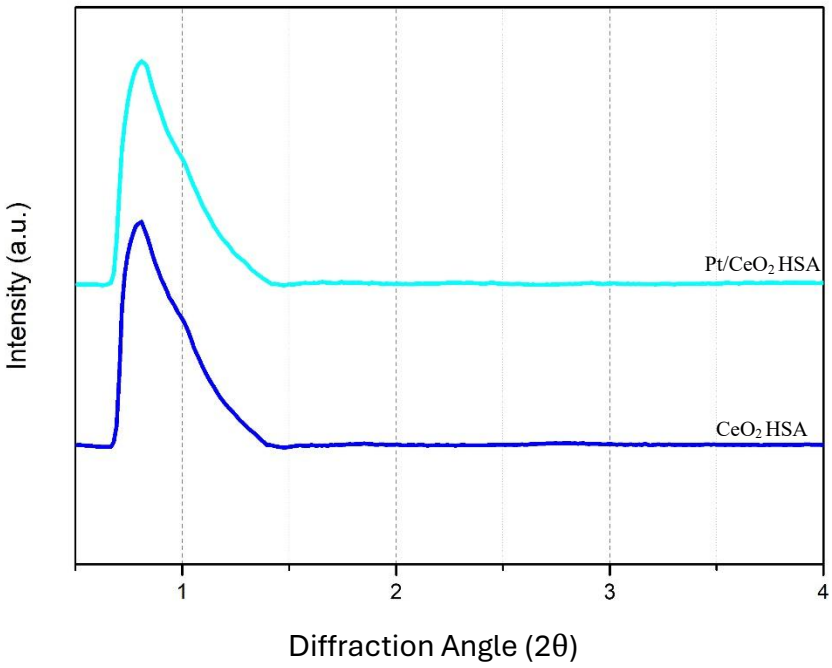

Figure 3.8. XRD patterns associated to Pt/CeO_2 HSA and CeO_2 HSA in the low angle range.

Bragg relation (Equation 2.2) was used to determine d-spacings in the samples and to calculate the lattice parameter a, corrected through Nelson–Riley extrapolation (Equation 2.3). Finally, Sherrer relation (2.4) was used the average crystallite size C_s. Results are reported in Table 3.2.

Table 3.2. Lattice parameter a and crystallite size C_s for all the investigated samples.

Sample	a (Å)	C_s (nm)
CeO_2 LSA	5,4111	34
CeO_2 MSA	5,4106	11
CeO_2 HSA	5,4147	6
Pt/CeO_2 LSA	5,4077	35
Pt/CeO_2 MSA	5,4145	12
Pt/CeO_2 HSA	5,4109	6

The calculated lattice parameter a, is essentially constant among all the investigated samples, with variations remaining below 1%. Such a limited fluctuation indicates that the crystal structure of ceria is substantially preserved despite platinum addition. Moreover, obtained values are fully consistent with those commonly reported for fluorite-type CeO_2, whose lattice parameter is typically close to 5.41 Å. This suggests that the introduction of Pt does not significantly modify the dimensions of the ceria unit cell. [104]

From a structural standpoint, this behavior is reasonable. At low Pt loadings generally do not enter sufficiently to bulk ceria lattice to induce measurable cell distortion by XRD. This interpretation is coherent with the extensive literature on Pt/ CeO_2 systems, where the absence of significant lattice changes is frequently associated with low noble-metal loading and predominant surface dispersion rather than true bulk incorporation. [105]

A different trend is instead observed for the average crystallite size, C_s, which shows more evident variations among the samples. Nevertheless, the measured values remain within the range commonly reported for nanocrystalline ceria-based materials. This confirms that all the prepared solids retain a nanostructured character compatible with literature data. In the Pt-containing samples, a moderate increase in crystallite size can be observed. This trend should be interpreted cautiously. Rather than indicating a direct expansion of the CeO_2 unit cell, the increase more plausibly reflects a slight enhancement of crystal growth or crystallite coarsening during preparation and calcination, possibly promoted by the presence of platinum species or by local modifications in the surface energy and redox behavior of ceria. In other words, platinum may influence the evolution of crystallite dimensions without substantially altering the intrinsic fluorite lattice parameter. Given the very low Pt loading, however, this effect remains limited and does not imply a relevant change of the support, as clearly shown in Pt/CeO_2 HSA and CeO_2 HSA, which exhibit the same value of C_s [106]

3.1.4 H_2-TPR Results

The H_2-TPR analysis was conducted on all the synthesized samples. The obtained TCD signal versus temperature patterns are reported in Figure 3.9:

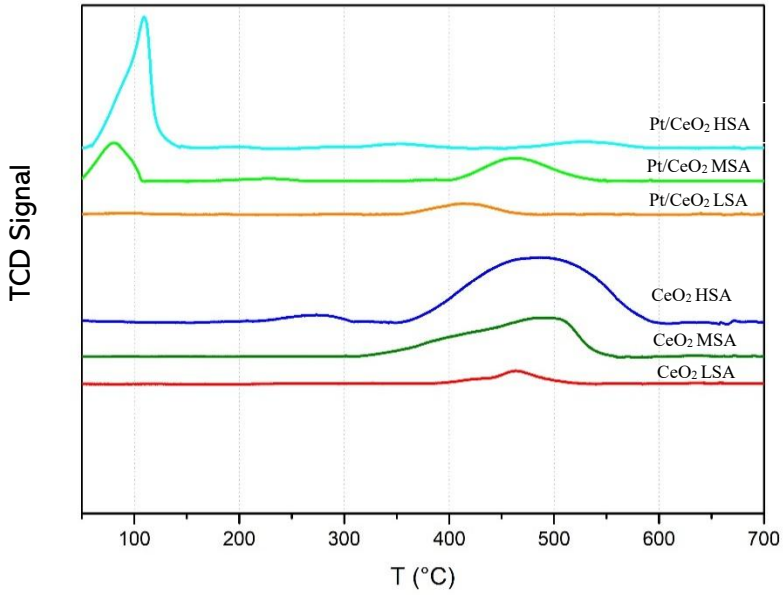

Figure 3.9. H_2-TPR of all investigated samples,

The H_2-TPR profiles of the Pt/CeO_2 HSA and Pt/CeO_2 MSA samples exhibit a low-temperature reduction feature below 100 °C, which can be attributed to the interaction of hydrogen with highly dispersed oxidized platinum species (PtO_X clusters). The intensity of this signal is also reasonably associated with the hydrogen spillover phenomenon, whereby molecular hydrogen dissociates on the platinum surface and migrates onto the ceria support. This process promotes the partial reduction of Ce^{4+} to Ce^{3+}, accompanied by the formation of oxygen vacancies and water. The absence of this low temperature peak in the Pt/CeO_2 LSA sample may suggest a lower platinum dispersion and, consequently, a less effective metal–support interfacial interaction. [107]

A reduction feature in the 400–500 °C range is observed for all samples and can be attributed to the surface and subsurface reduction of ceria. In this temperature interval, hydrogen reacts with lattice oxygen at the ceria surface, producing water and generating oxygen vacancies, while nearby Ce^{4+} reduces to Ce^{3+}. More specifically, as the reduction proceeds, the most accessible surface oxygen atoms are progressively removed, and the process extends under the external layer. Consequently, subsurface oxygen species migrate toward the surface to refill the newly created vacancies, where they can further react with hydrogen and be released as water. The signal observed in this region therefore reflects a combined process of oxygen removal, vacancy formation, Ce^{4+} Ce^{3+} redox transformation, and oxygen mobility between surface and subsurface layers, all of which are characteristic of the redox behavior of ceria under hydrogen. [108]

In the CeO_2 HSA sample, a weak reduction peak is also detectable at approximately 300 °C. This feature may reasonably be ascribed to the reduction of surface ceria species, likely influenced by the interaction between CeO_2 and the traces the SBA-15 template, confirmed

even from XRD analysis. Such behavior appears consistent with reduction features reported in the literature for ceria-containing SBA-15. [109]

From the integration of the peaks, the total quantity of reduced hydrogen was calculated in terms of μmol of hydrogen on grams of catalyst. Results are reported in the Table 3.3:

Table 3.3. Hydrogen reduced in H_2-TPR,

Sample	H_2 consumption at T < 200°C ($\mu molH_2/g$)	H_2 consumption at T > 200°C ($\mu molH_2/g$)
CeO_2 LSA	-	47.4
CeO_2 MSA	-	318.9
CeO_2 HSA	-	414.47
Pt/CeO_2 LSA	5.4	72.5
Pt/CeO_2 MSA	35.3	215.8
Pt/CeO_2 HSA	280.4	135.2

The hydrogen consumption values are in good agreement with the H_2-TPR profiles. Bare ceria samples do not exhibit significant reduction below 200 °C, whereas Pt-containing catalysts show a distinct low-temperature hydrogen uptake, attributable to the presence of platinum and to hydrogen spillover from Pt to the ceria surface.

Considering the Pt loading of 0.5 wt%, the total platinum content corresponds to approximately 25.6 μmol Pt g^{-1}. Assuming that platinum is initially present as oxidized species (PtO_x) and that the reduction proceeds according to a 1:1 stoichiometric ratio between Pt and H_2 ($PtO + H_2 \rightarrow Pt + H_2O$), the theoretical hydrogen consumption associated with the complete reduction of Pt species would be about 25.6 μmol H_2 g^{-1}. The experimental H_2 consumption associated at the low temperature peak (around 100 °C) of Pt/CeO_2 LSA is significantly lower, amounting to about 5.22 μmol H_2 g^{-1}, which suggests that only a fraction of the total platinum species is present as reducible oxidized sites under the experimental conditions. The remaining platinum strongly interacting with the ceria support or are not accessible, thus not contributing significantly to the H_2 consumption during the TPR experiment.

On the other hand, the spillover effect is particularly pronounced for Pt/CeO_2 HSA, which displays the highest low-temperature consumption, indicating a stronger metal-support interaction and a more effective activation of reducible surface oxygen. At higher temperatures, hydrogen consumption is mainly associated with the reduction of ceria itself, with the support samples showing increasing reducibility as the surface area increases.

3.1.5 CO Chemisorption Results

The CO chemisorption test, described in the previous section, was conducted on all the Platinum based samples (Pt/CeO_2 LSA, Pt/CeO_2 MSA, Pt/CeO_2 HSA) and enabled the determination of two key parameters related to the platinum phase, namely the metal dispersion d_{is} and the equivalent hemispherical particle diameter D. The corresponding values are reported in Table 3.4.

Table 3.4. metal dispersion d_{is} and equivalent hemispherical particle diameter D for all Pt-samples.

Sample	d_{is}	D (nm)
Pt/CeO_2 LSA	13%	9.43
Pt/CeO_2 MSA	56%	2.13
Pt/CeO_2 HSA	81%	1.47

Satisfactory values of metal dispersion were obtained for all the platinum-containing samples, with the highest value being observed for Pt/CeO_2 HSA (81%). Such a result confirms the successful deposition of platinum nanoparticles onto the ceria surface and indicates that the metal phase is highly dispersed, with a significant fraction of Pt atoms exposed to the catalyst surface.

Conversely, the lower dispersion values observed for Pt/CeO_2 LSA and Pt/CeO_2 MSA are reasonably attributable to the minor specific surface area of these samples, as highlighted by BET measurements. A less developed surface area reduces the number of available deposition sites and may favor particle growth and/or agglomeration, decreasing the fraction of exposed platinum atoms. Overall, the CO chemisorption data are fully consistent with the textural properties previously discussed and compatible with data reported in literature. [96]

3.2 Catalytic Test results

In this section, the catalytic performance of the synthesized materials will be discussed. The analysis will begin with the results of the CO oxidation tests, used as a probe molecule for VOC oxidation. Subsequently, the catalytic behavior in ethylene oxidation will be examined. Finally, the results of TOS tests will be presented and discussed in order to assess the durability of the catalysts under prolonged operating conditions.

3.2.1 CO oxidation Test

The CO oxidation tests provide a first assessment of the catalytic activity toward a model oxidation reaction. Figure 3.10 exhibits the CO conversions as a function of temperature for supports samples (CeO_2 LSA, CeO_2 MSA, CeO_2 HSA).

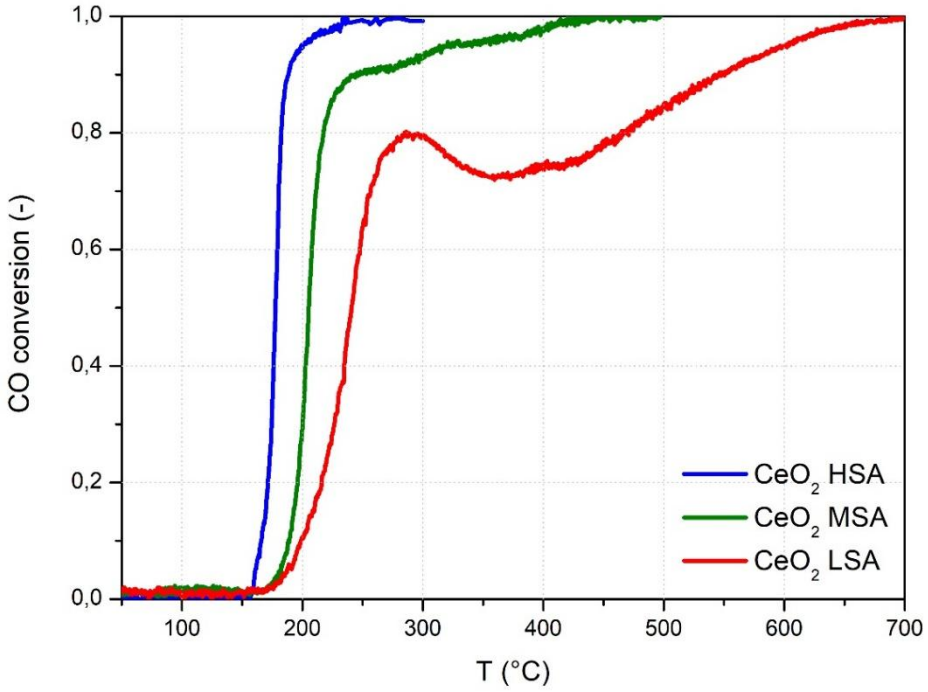

Figure 3.10. CO conversion versus Temperature for CeO_2 supports.

Figure 3.10 illustrates the activity of Ceria supports towards CO oxidation, through mechanism and reaction pathways already discussed. In the CeO_2 LSA, an anomalous peak of conversion is reported before 300°C, imputable to the formation of carbonaceous byproducts or their desorption. [110]

In the Table 3.5, relevant catalyst parameters are reported, as T_{10}, T_{50}, T_{90}, which are temperature to achieve 10%, 50%, 90% of CO conversion, respectively.

Table 3.5 T_{10}, T_{50}, T_{90} for supports in CO oxidation

Sample	T_{10} (°C)	T_{50} (°C)	T_{90} (°C)
CeO_2 LSA	200	240	550
CeO_2 MSA	189	205	245
CeO_2 HSA	166	178	188

The catalytic activity is confirmed to be higher in samples at higher superficial area and the presence of higher numbers of defects. In particular, the increase in surface area likely promotes a greater availability of accessible active sites and enhances the interaction between the reactant molecules and the ceria surface. For instance, it is interesting to underline the good performance of only CeO_2 HSA, able to achieve a complete CO conversion at 300°C.

The catalytic activity improves drastically in the presence of Platinum nanoparticles, as exhibited in the Figure 3.11.

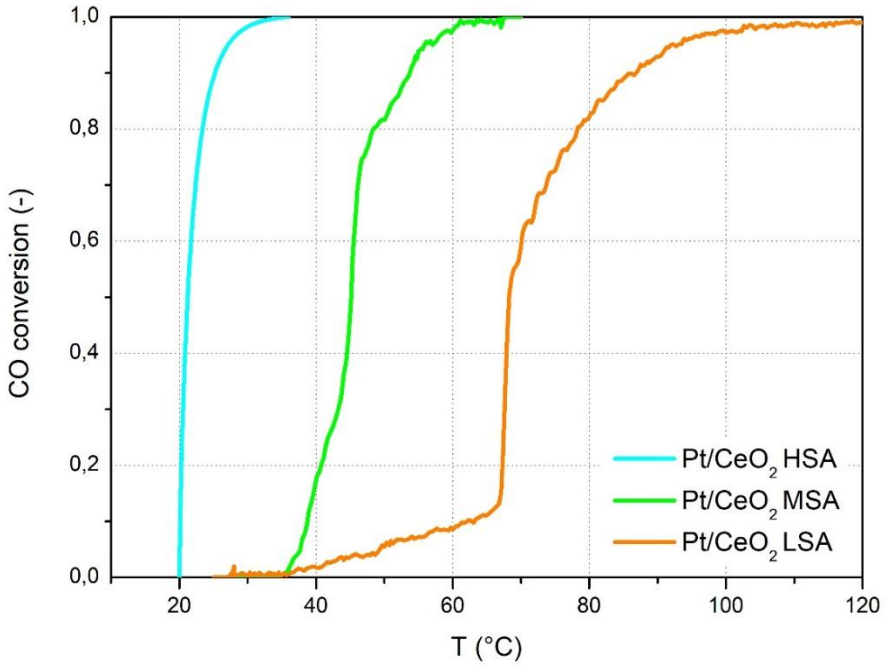

Figure 3.11. CO conversion versus Temperature for Pt/CeO_2 samples.

Due to the presence of the active metal phase (Pt) and to the synergistic effect of Pt and Ceria, already discussed in previous sections, all Pt/CeO_2 samples exhibited outstanding catalytic performances over a lower temperature range.

Among them, Pt/CeO_2 HSA displayed the best behavior, with an extremely sharp increase in CO conversion occurring at very low temperature. In this case, the oxidation reaction proceeded so rapidly that an accurate determination of the T_{10} and T_{50} values was not feasible. Nevertheless, the sample reached complete CO conversion around 36°C, that is, close to room temperature, clearly demonstrating its remarkable catalytic efficiency thanks to platinum nanoparticles and ceria vacancies. Temperatures corresponding to relevant value of conversion are reported in Table 3.6

Table 3.6 T_{10}, T_{50}, T_{90}, for Pt/CeO_2 in CO oxidation.

Sample	T_{10} (°C)	T_{50} (°C)	T_{90} (°C)
Pt/CeO_2 LSA	62	68	87
Pt/CeO_2 MSA	38	45	54
Pt/CeO_2 HSA	-	-	25

3.2.2 Ethylene Catalytic Tests

Ethylene Catalytic Tests were performed in order to assess an evaluation of the oxidation capabilities of the samples toward a more complex reactant. In this test the role of Platinum is even more remarkable. Indeed, Figure 3.12 exhibits ethylene conversion as a function of temperature for bare ceria supports.

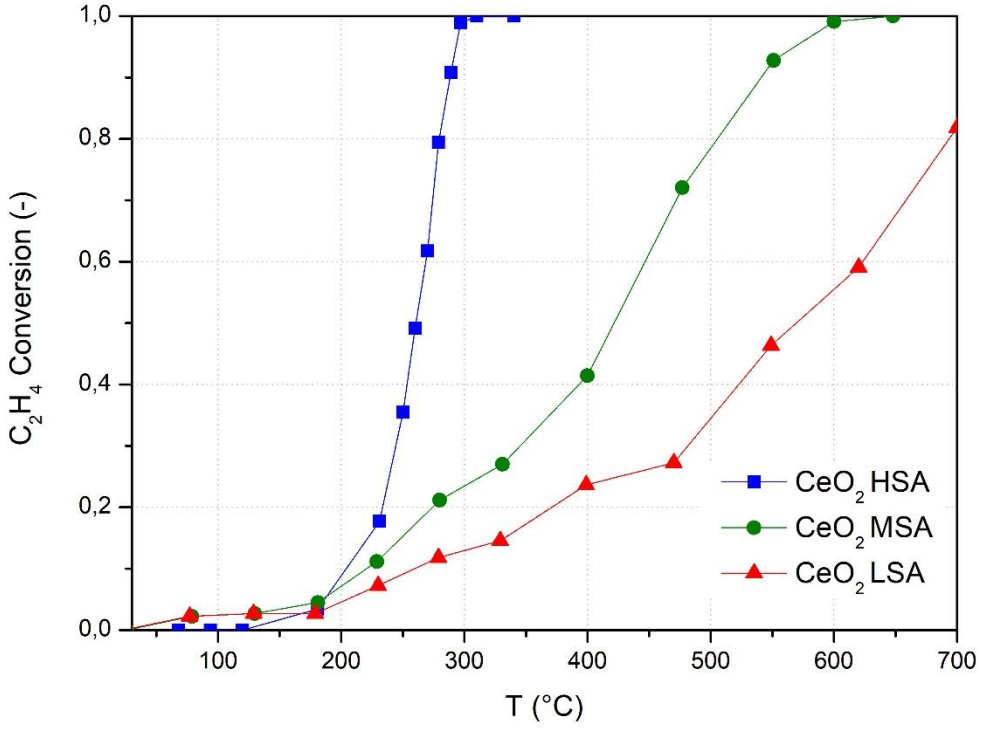

Figure 3.12. C_2H_4 conversion vs temperature for CeO_2 supports.

In this case, all the samples exhibit relevant activity at a $T > 200°C$. The best performance was guaranteed by the high surface area support, CeO_2 HSA, able to reach a conversion equal to 100% around 310°C. Conversely, CeO_2 LSA displayed the lowest activity among the investigated samples and was not able to achieve complete ethylene conversion within the explored temperature range of 0-750°C. Table 3.7 sums the temperature associated with relevant values of conversion.

Table 3.7 T_{10}, T_{50}, T_{90} for supports in C_2H_4 oxidation.

Sample	T_{10} (°C)	T_{50} (°C)	T_{90} (°C)
CeO_2 LSA	275	560	750
CeO_2 MSA	228	420	550
CeO_2 HSA	200	260	288

The presence of Platinum shifts the conversion profiles toward lower temperatures and significantly enhances the overall catalytic activity, in agreement with the synergistic effects

established between platinum and ceria, as discussed previously. The conversion profiles are shown in Figure 3.13.

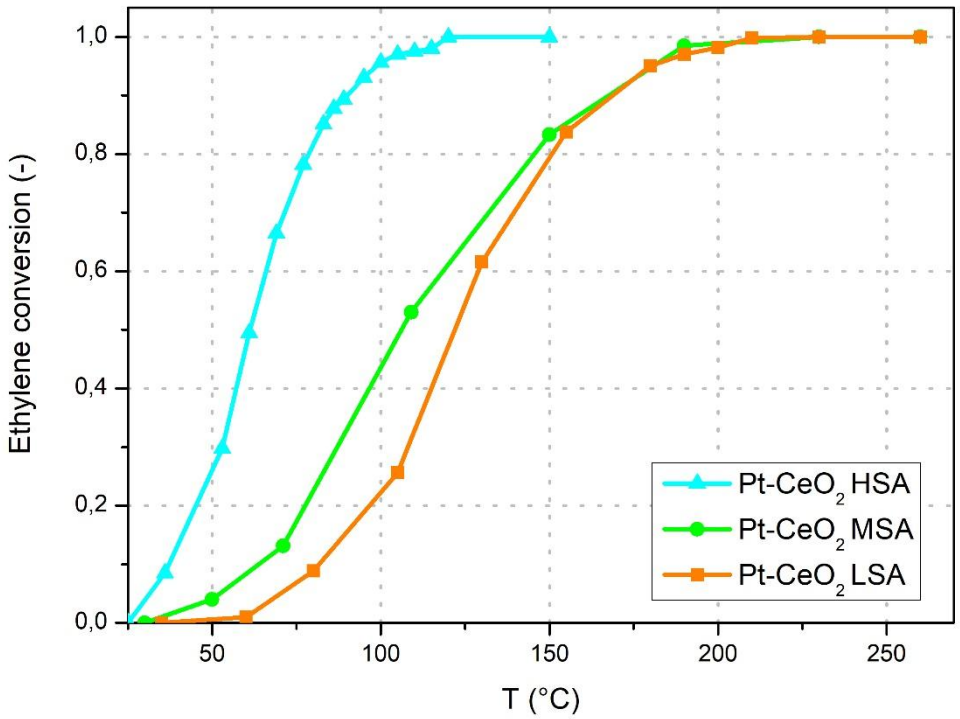

Figure 3.13. C_2H_4 conversion versus Temperature for Pt/CeO_2 samples.

Pt/CeO_2 MSA exhibited slightly better catalytic performance than Pt/CeO_2 LSA especially at temperatures below 150 °C, a result that can be mainly attributed to its higher platinum dispersion and larger accessible active surface area. Also in this case, the sample characterized by the highest specific surface area, namely Pt/CeO_2 HSA showed the best catalytic behavior, achieving complete ethylene conversion at 110°C. Table 3.8 reports the temperature associated with relevant values of conversion.

Table 3.8 7 T_{10}, T_{50}, T_{90} for supports in C_2H_4 oxidation

Sample	T_{10} (°C)	T_{50} (°C)	T_{90} (°C)
Pt/CeO_2 LSA	80	125	180
Pt/CeO_2 MSA	70	109	170
Pt/CeO_2 HSA	37	61	89

Turnover frequency (TOF) was calculated for the three catalysts in order to achieve a more rigorous assessment of their catalytic efficiency and reaction kinetics. A temperature of 50°C was selected to ensure low conversion levels for all the catalysts (under the 30%)

allowing a more reliable assessment of their intrinsic activity under conditions where heat and mass transfer limitations can be reasonably neglected. Under these conditions, the measured reaction rates more accurately reflect the nature and effectiveness of the active sites.[111] The calculated TOF values are reported in Table 3.8.

Table 3.8. TOF values for platinum based samples in C_2H_4 oxidation reaction.

Sample	TOF (s^{-1})
Pt/CeO_2 LSA	$6.30 \cdot 10^{-5}$
Pt/CeO_2 MSA	$1.9 \cdot 10^{-4}$
Pt/CeO_2 HSA	$1.0 \cdot 10^{-3}$

The reported TOF values are consistent with those commonly described in the heterogeneous catalysis literature [112]. Notably, Pt/CeO_2 HSA exhibits a TOF more than one order of magnitude higher than that of Pt/CeO_2 MSA and approximately two orders of magnitude higher than that of Pt/CeO_2 LSA. This marked difference accounts for its superior catalytic performance and enhanced activity, in agreement with the results previously discussed.

3.2.3 Time on stream tests results

The Time on Stream (TOS) tests were carried out to evaluate the stability of the catalytic performance under continuous reaction conditions.

For the CO oxidation reaction, the catalyst exhibiting the lowest activity among the investigated samples, Pt/CeO_2 LSA, was intentionally selected in order to assess its behavior under demanding conditions. The experiment was conducted at a temperature of 79°C, corresponding to an initial CO conversion of approximately 80%, for 24 hours, as shown in Figure 3.14.

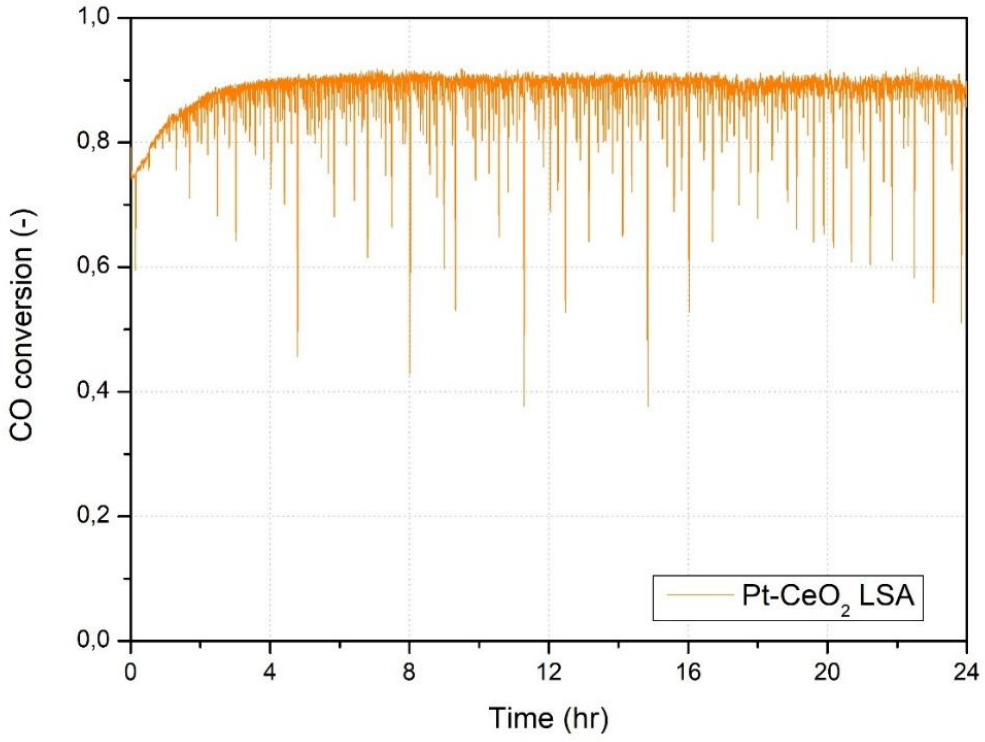

Figure 3.14. CO conversion versus temperature in TOS Test on Pt/CeO_2 LSA.

During the TOS experiment, the catalyst exhibited a pronounced oscillatory behavior, with the conversion fluctuating within a range of approximately 40% to 85%. Such oscillatory phenomena have been widely reported in the literature for CO oxidation over Pt/CeO_2 catalytic systems.

Furthermore, previous studies have demonstrated that Pt nanoparticles supported on ceria can exhibit intense fluxional behavior in the presence of CO, particularly at low temperatures. Under these conditions, the adsorption of CO molecules induces structural and electronic perturbations at the metal-support interface, promoting the removal of lattice oxygen atoms and temporarily destabilizing the Pt nanoparticles. As a result, the catalytic surface undergoes continuous structural rearrangements, which manifest macroscopically as oscillations in the observed CO conversion during the reaction. [113], [114]

Focusing on ethylene oxidation, the best catalyst was selected in this case, Pt/CeO_2 HSA, selecting a temperature of 80°C, able to ensure the 75% of initial ethylene conversion. The test was conducted for 24 hours and the results are reported in Figure 3.15.

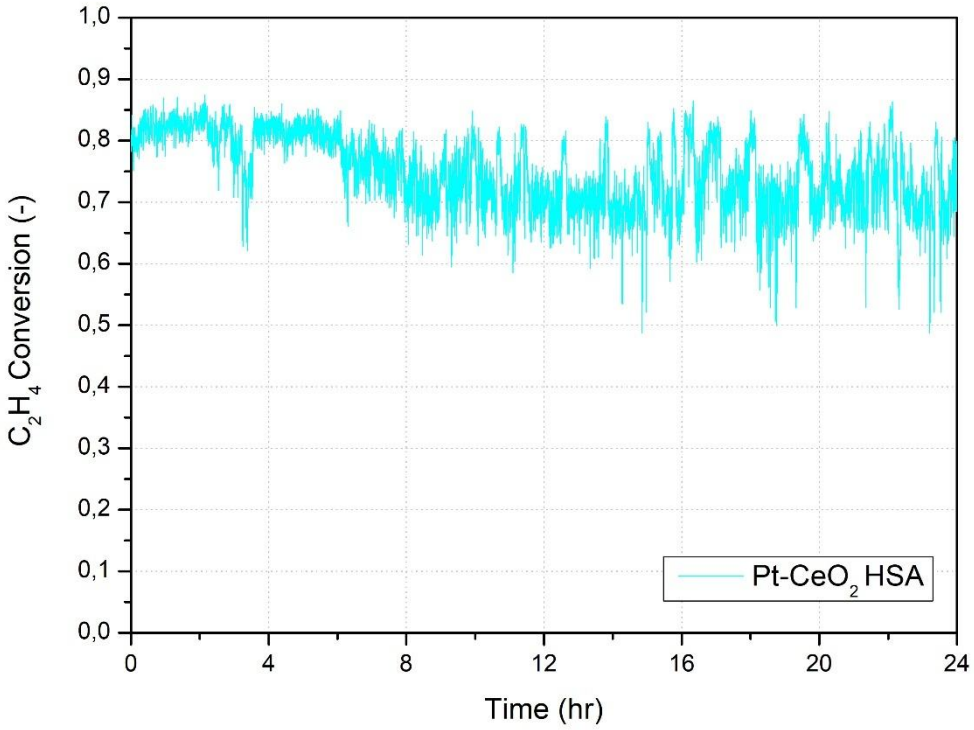

Figure 3.14. C_2H_4 conversion versus temperature in TOS Test on Pt/CeO_2 HSA.

During the course of the experiment, the catalyst maintained a generally stable catalytic performance, confirming the good stability of the Pt/CeO_2 HSA system under continuous reaction conditions. However, a certain degree of oscillatory behavior in the conversion values was observed throughout the test. Compared with the oscillations previously observed during CO oxidation, the fluctuations in the ethylene oxidation experiment appear to be significantly less pronounced and characterized by a lower amplitude.

For this reason, the observed oscillations are more plausibly attributable to instrumental noise or minor fluctuations in the experimental conditions, rather than to intrinsic catalytic phenomena related to the reaction mechanism or to dynamic restructuring of the catalyst surface. This interpretation is consistent with the generally more stable kinetic behavior typically reported for ethylene oxidation on Pt-based catalysts under comparable operating conditions.

However, it is worth noting that in the final phase of the experiment, particularly in the time interval between 18 and 24 hours, the oscillations become slightly more evident. During this period, the ethylene conversion fluctuates within a range between 50% and 85%. Although these variations remain limited and do not indicate any clear trend of catalyst deactivation, they may suggest the occurrence of minor transient effects, possibly associated with small variations in gas flow, temperature control, or detector sensitivity.

4. Conclusions

In the present dissertation, six different catalytic systems were synthesized, tested, and characterized, including three ceria supports and three platinum-loaded ceria catalysts, with the aim of assessing their activity and stability toward VOC oxidation. The study was specifically designed to investigate how variations in textural properties, such as specific surface area and pore size distribution, influence catalytic performance, while maintaining a constant platinum loading equal to 0.5%. The latter was selected in order to ensure an appropriate compromise between catalytic activity and economic sustainability.

Two of the supports, namely CeO_2 LSA and CeO_2 MSA, were prepared by solution combustion synthesis (SCS). Different thermal treatments were subsequently applied in order to obtain materials with distinct surface areas and textural characteristics. The third support, CeO_2 HSA, was synthesized using mesoporous silica SBA-15 as a hard template, with the purpose of achieving the highest specific surface area among the investigated samples. Platinum nanoparticles were then deposited via stirring at room temperature onto each support, yielding the corresponding catalysts Pt/CeO_2 LSA, Pt/CeO_2 MSA and Pt/CeO_2 HSA.

Regarding characterization, the platinum nanoparticles were first analyzed by TEM in order to determine their size distribution. The analysis revealed an average particle diameter of 1.83 nm, consistent with the intended nanoscale dimensions and therefore favorable for achieving high dispersion on the support surface. Textural properties, including specific surface area and pore dimensions, were investigated by BET analysis. The results confirmed that Pt/CeO_2 HSA exhibited the highest specific surface area, reaching 122.6 m^2/g.

Additional structural information was obtained by XRD analysis, which confirmed the fluorite structure of CeO_2 in all samples and also revealed the presence of residual SBA-15 in the Pt/CeO_2 HSA and CeO_2 HSA materials. CO chemisorption was employed to evaluate platinum dispersion on the supports, a key parameter in catalysis because it directly affects the exposed noble metal surface area and, consequently, the number of accessible active sites. In this respect, satisfactory dispersion values were obtained in the case of higher surface are samples, with 56% for Pt/CeO_2 MSA and 81% for Pt/CeO_2 HSA.

Finally, H_2-TPR analysis was carried out to investigate the reducibility of the samples and their hydrogen consumption. Peak integration allowed the quantification of hydrogen uptake, suggesting that only a fraction of the total platinum species was present as reducible oxidized sites. At the same time, the results pointed to the occurrence of a significant hydrogen spillover effect and easily reducible ceria, particularly pronounced in the Pt/CeO_2 HAS sample.

Catalytic tests were performed to assess the activity of the synthesized materials toward the oxidation of two representative compounds, CO and C_2H_4, chosen as probe molecules for the evaluation of VOC oxidation performance. The results obtained on the bare supports emphasized the decisive contribution of platinum to the catalytic behavior of the systems. The promoting effect of Pt is associated not only with its intrinsic catalytic activity in oxidation reactions, but also with its capability to activate oxygen and to enhance the reducibility and oxygen transfer properties of ceria through metal–support interactions at the Pt/CeO_2 interface.

In fact, all platinum containing catalysts exhibited significantly improved activity compared with the corresponding supports, especially in the low-temperature region. In particular, Pt/CeO_2 HSA showed the best performance, reaching a T_{90} of 25 °C for CO oxidation and

89 °C for C_2H_4 oxidation. Such low T_{90} values demonstrate the excellent catalytic efficiency of this material and underline the beneficial effect of combining platinum with a high surface area and defect-rich ceria support.

This enhanced behavior can be attributed to a synergistic combination of factors, including the high dispersion of platinum nanoparticles, the larger specific surface area of the support, and the improved availability of active interfacial sites. These features promote adsorption and activation of the reactants while also facilitating lattice oxygen participation and vacancy regeneration, both of which are essential for oxidation processes on ceria-based catalysts. Furthermore, the TOF value associated to Pt/CeO_2 HSA, in the order of 10^{-3} s^{-1}, are in agreement with those generally reported in the heterogeneous catalysis literature for efficient noble-metal oxidation catalysts, including systems of potential industrial relevance.

To conclude, time on stream (TOS) tests were performed in order to evaluate the stability of the catalytic performance under prolonged reaction conditions. Two representative samples were selected for these experiments: Pt/CeO_2 LSA for CO oxidation and Pt/CeO_2 HSA for C_2H_4 oxidation.

In the case of CO oxidation, the Pt/CeO_2 LSA catalyst exhibited noticeable oscillations in conversion during the test. Although these fluctuations indicate a less stable catalytic response, the catalyst nevertheless maintained a measurable level of activity throughout the experiment. Such oscillatory behavior may be related to transient surface phenomena, including periodic changes in the coverage of adsorbed species or local variations in the oxidation state of the active sites.

By contrast, Pt/CeO_2 HSA displayed a more stable behavior during the oxidation of C_2H_4 with less pronounced oscillations in conversion over time. This result suggests better resistance to deactivation and a more robust catalytic performance under extended operating conditions. The improved stability of this sample can reasonably be associated with its higher surface area, better platinum dispersion, and stronger metal–support interaction, all of which contribute to maintaining the availability of active sites during prolonged reaction times.

Catalytic tests results indicate that Pt/CeO_2 HSA combines high catalytic activity with superior stability, thus confirming its potential as the most promising catalyst among the investigated materials for low temperature oxidation applications.

5. Bibliography

[1] P. Pandey and R. Yadav, "A Review on Volatile Organic Compounds (VOCs) as Environmental Pollutants: Fate and Distribution," *INTERNATIONAL JOURNAL OF PLANT AND ENVIRONMENT*, vol. 4, no. 02, pp. 14–26, Jul. 2018, doi: 10.18811/ijpen.v4i02.2.

[2] A. Guenther, "Seasonal and spatial variations in natural volatile organic compound emissions," 1997, *Ecological Society of America*. doi: 10.1890/1051-0761(1997)007[0034:SASVIN]2.0.CO;2.

[3] F. Tassi *et al.*, "Geogenic and atmospheric sources for volatile organic compounds in fumarolic emissions from Mt. Etna and Vulcano Island (Sicily, Italy)," *Journal of Geophysical Research Atmospheres*, vol. 117, no. 17, 2012, doi: 10.1029/2012JD017642.

[4] P. Ciccioli, M. Centritto, and F. Loreto, "Biogenic volatile organic compound emissions from vegetation fires," 2014, *Blackwell Publishing Ltd*. doi: 10.1111/pce.12336.

[5] B. Yuan *et al.*, "Emissions of volatile organic compounds (VOCs) from concentrated animal feeding operations (CAFOs): Chemical compositions and separation of sources," *Atmos. Chem. Phys.*, vol. 17, no. 8, pp. 4945–4956, Apr. 2017, doi: 10.5194/acp-17-4945-2017.

[6] G. A. Novak and T. H. Bertram, "Reactive VOC Production from Photochemical and Heterogeneous Reactions Occurring at the Air-Ocean Interface," *Acc. Chem. Res.*, vol. 53, no. 5, pp. 1014–1023, May 2020, doi: 10.1021/acs.accounts.0c00095.

[7] N. K. Cheruyiot *et al.*, "An overview: Polycyclic aromatic hydrocarbon emissions from the stationary and mobile sources and in the ambient air," Dec. 01, 2015, *AAGR Aerosol and Air Quality Research*. doi: 10.4209/aaqr.2015.11.0627.

[8] P. Wang and W. Zhao, "Assessment of ambient volatile organic compounds (VOCs) near major roads in urban Nanjing, China," *Atmos. Res.*, vol. 89, no. 3, pp. 289–297, Aug. 2008, doi: 10.1016/j.atmosres.2008.03.013.

[9] C. H. Halios, C. Landeg-Cox, S. D. Lowther, A. Middleton, T. Marczylo, and S. Dimitroulopoulou, "Chemicals in European residences – Part I: A review of emissions, concentrations and health effects of volatile organic compounds (VOCs)," Sep. 15, 2022, *Elsevier B.V.* doi: 10.1016/j.scitotenv.2022.156201.

[10] U. Schlink, M. Rehwagen, M. Damm, M. Richter, M. Borte, and O. Herbarth, "Seasonal cycle of indoor-VOCs: Comparison of apartments and cities," *Atmos. Environ.*, vol. 38, no. 8, pp. 1181–1190, 2004, doi: 10.1016/j.atmosenv.2003.11.003.

[11] R. Meininghaus, L. Gunnarsen, and H. N. Knudsen, "Diffusion and sorption of volatile organic compounds in building materials - Impact on indoor air

quality," *Environ. Sci. Technol.*, vol. 34, no. 15, pp. 3101–3108, Aug. 2000, doi: 10.1021/es991291i.

[12] E. Gallego, X. Roca, J. F. Perales, and X. Guardino, "Determining indoor air quality and identifying the origin of odour episodes in indoor environments," *Journal of Environmental Sciences*, vol. 21, no. 3, pp. 333–339, 2009, doi: 10.1016/S1001-0742(08)62273-1.

[13] X. Tang, P. K. Misztal, W. W. Nazaroff, and A. H. Goldstein, "Volatile organic compound emissions from humans indoors," *Environ. Sci. Technol.*, vol. 50, no. 23, pp. 12686–12694, Dec. 2016, doi: 10.1021/acs.est.6b04415.

[14] T. Horvat, G. Pehnec, and I. Jakovljević, "Volatile Organic Compounds in Indoor Air: Sampling, Determination, Sources, Health Risk, and Regulatory Insights," May 01, 2025, *Multidisciplinary Digital Publishing Institute (MDPI)*. doi: 10.3390/toxics13050344.

[15] L. F. Liotta, "Catalytic oxidation of volatile organic compounds on supported noble metals," Oct. 20, 2010. doi: 10.1016/j.apcatb.2010.08.023.

[16] E. Cetin, M. Odabasi, and R. Seyfioglu, "Ambient volatile organic compound (VOC) concentrations around a petrochemical complex and a petroleum refinery," *Science of the Total Environment*, vol. 312, no. 1–3, pp. 103–112, Aug. 2003, doi: 10.1016/S0048-9697(03)00197-9.

[17] A. Ragothaman and W. A. Anderson, "Air quality impacts of petroleum refining and petrochemical industries," Sep. 01, 2017, *MDPI AG*. doi: 10.3390/environments4030066.

[18] C. Y. Hsu *et al.*, "Ambient VOCs in residential areas near a large-scale petrochemical complex: Spatiotemporal variation, source apportionment and health risk," *Environmental Pollution*, vol. 240, pp. 95–104, Sep. 2018, doi: 10.1016/j.envpol.2018.04.076.

[19] D. Saraga, S. Pateraki, A. Papadopoulos, C. Vasilakos, and T. Maggos, "Studying the indoor air quality in three non-residential environments of different use: A museum, a printery industry and an office," *Build. Environ.*, vol. 46, no. 11, pp. 2333–2341, Nov. 2011, doi: 10.1016/j.buildenv.2011.05.013.

[20] X. Guo, Q. Lei, X. Li, J. Chen, and C. Yi, "A Visualized Analysis of Research Hotspots and Trends on the Ecological Impact of Volatile Organic Compounds," *Atmosphere (Basel).*, vol. 16, no. 8, Aug. 2025, doi: 10.3390/atmos16080900.

[21] S. Solomon, "Stratospheric ozone depletion: A review of concepts and history," 1999, *Blackwell Publishing Ltd*. doi: 10.1029/1999RG900008.

[22] D. M. Pinto, J. D. Blande, S. R. Souza, A. M. Nerg, and J. K. Holopainen, "Plant volatile organic compounds (vocs) in ozone (o 3) polluted atmospheres: The ecological effects," *J. Chem. Ecol.*, vol. 36, no. 1, pp. 22–34, Feb. 2010, doi: 10.1007/s10886-009-9732-3.

[23] E.-H. Choi, "Estimation of Indirect Greenhouse Effect by Non-methane Volatile Organic Compounds," *Journal of Environmental Science*

International, vol. 21, no. 2, pp. 165–179, Feb. 2012, doi: 10.5322/jes.2012.21.2.165.

[24] J. E. Colman Lerner, M. A. Peluso, M. A. Campesi, H. J. Thomas, A. A. Porta, and J. E. Sambeth, "INFLUENCE OF VOC EMISSIONS ON GLOBAL WARMING. MITIGATION OF THEIR IMPACT USING CERAMIC MONOLITHS SUPPORTED Pt, Mn AND Ce CATALYSTS AT PILOT SCALE," 2017.

[25] X. Zhou, X. Zhou, C. Wang, and H. Zhou, "Environmental and human health impacts of volatile organic compounds: A perspective review," *Chemosphere*, vol. 313, Feb. 2023, doi: 10.1016/j.chemosphere.2022.137489.

[26] A. Sperti, "Il codice dell'ambiente (d.lgs. 152/2006)," in *[Attuazione della Costituzione : recenti riforme e ipotesi di revisione. - (Didattica e ricerca. Manuali)]*, Pisa: PLUS-Pisa University Press, 2006. [Online]. Available: http://digital.casalini.it/10.1400/126032

[27] K. Rumchev, H. Brown, and J. Spickett, "Volatile Organic Compounds: Do they present a risk to our health?," 2007.

[28] C. J. Weschler and H. C. Shields, "POTENTIAL REACTIONS AMONG INDOOR POLLUTANTS," 1997.

[29] G. P. Pappas, R. J. Herbert, W. Henderson, J. Koenig, B. Stover, and S. Barnhart, "The Respiratory Effects of Volatile Organic Compounds," *Int. J. Occup. Environ. Health*, vol. 6, no. 1, pp. 1–8, Jan. 2000, doi: 10.1179/oeh.2000.6.1.1.

[30] L. Chen, G. Hu, R. Fan, Y. Lv, Y. Dai, and Z. Xu, "Association of PAHs and BTEX exposure with lung function and respiratory symptoms among a nonoccupational population near the coal chemical industry in Northern China," *Environ. Int.*, vol. 120, pp. 480–488, Nov. 2018, doi: 10.1016/j.envint.2018.08.004.

[31] G. Gałezowska, M. Chraniuk, and L. Wolska, "In vitro assays as a tool for determination of VOCs toxic effect on respiratory system: A critical review," Mar. 01, 2016, *Elsevier B.V.* doi: 10.1016/j.trac.2015.10.012.

[32] T. Salthammer, S. Mentese, and R. Marutzky, "Formaldehyde in the indoor environment," *Chem. Rev.*, vol. 110, no. 4, pp. 2536–2572, Apr. 2010, doi: 10.1021/cr800399g.

[33] C. W Tam, R. J Bevan, P. T C Harrison, L. C Youngs, and D. Crump, "Public Health Impacts of Exposure to Carbon Monoxide From Gas Appliances in UK Homes – Are We Missing Something?," *Indoor and Built Environment*, vol. 21, no. 2, pp. 229–240, Dec. 2011, doi: 10.1177/1420326X11417980.

[34] J. A. Raub, "Health e□ects of exposure to ambient carbon monoxide."

[35] J. A. Raub, M. Mathieu-Nolf, N. B. Hampson, and S. R. Thom, "Carbon monoxide poisoning-a public health perspective," 2000. [Online]. Available: www.elsevier.com/locate/toxicol

[36] W. T. Tsai, “A Survey on Toxic Volatile Organic Compounds (VOCs): Toxicological Profiles, Health Exposure Risks, and Regulatory Strategies for Mitigating Emissions from Stationary Sources in Taiwan,” *Atmosphere (Basel).*, vol. 14, no. 2, Feb. 2023, doi: 10.3390/atmos14020242.

[37] J. M. Delgado-Saborit, N. J. Aquilina, C. Meddings, S. Baker, and R. M. Harrison, “Relationship of personal exposure to volatile organic compounds to home, work and fixed site outdoor concentrations,” *Science of the Total Environment*, vol. 409, no. 3, pp. 478–488, Jan. 2011, doi: 10.1016/j.scitotenv.2010.10.014.

[38] R. C. Spear and S. Selvin, “OSHA’s Permissible Exposure Limits: Regulatory Compliance Versus Health Risk,” *Risk analysis*, vol. 9, no. 4, pp. 579–586, 1989, doi: 10.1111/j.1539-6924.1989.tb01268.x.

[39] A. Bhaskaran, D. Sharma, S. Roy, and S. A. Singh, “Technological solutions for NOx, SOx, and VOC abatement: recent breakthroughs and future directions,” Aug. 01, 2023, *Springer Science and Business Media Deutschland GmbH*. doi: 10.1007/s11356-023-28840-y.

[40] A. S. Rodriguez Castillo, P. F. Biard, S. Guihéneuf, L. Paquin, A. Amrane, and A. Couvert, “Assessment of VOC absorption in hydrophobic ionic liquids: Measurement of partition and diffusion coefficients and simulation of a packed column,” *Chemical Engineering Journal*, vol. 360, pp. 1416–1426, Mar. 2019, doi: 10.1016/j.cej.2018.10.146.

[41] X. Li, L. Zhang, Z. Yang, P. Wang, Y. Yan, and J. Ran, “Adsorption materials for volatile organic compounds (VOCs) and the key factors for VOCs adsorption process: A review,” *Sep. Purif. Technol.*, vol. 235, Mar. 2020, doi: 10.1016/j.seppur.2019.116213.

[42] W. K. Pui, R. Yusoff, and M. K. Aroua, “A review on activated carbon adsorption for volatile organic compounds (VOCs),” Jul. 01, 2019, *De Gruyter*. doi: 10.1515/revce-2017-0057.

[43] R. F. Dunn and M. M. El-Halwagi, “Selection of optimal VOC-condensation systems,” *Waste Management*, vol. 14, no. 2, pp. 103–113, Jan. 1994, doi: 10.1016/0956-053X(94)90003-5.

[44] T. K. Poddar, S. Majumdar, and K. K. Sirkar, “Removal of VOCs from air by membrane-based absorption and stripping,” 1996.

[45] D. A. Lewandowski, *Design of thermal oxidation systems for volatile organic compounds*. CRC press, 2017.

[46] C. He, J. Cheng, X. Zhang, M. Douthwaite, S. Pattisson, and Z. Hao, “Recent Advances in the Catalytic Oxidation of Volatile Organic Compounds: A Review Based on Pollutant Sorts and Sources,” Apr. 10, 2019, *American Chemical Society*. doi: 10.1021/acs.chemrev.8b00408.

[47] A. Datta and L. Philip, “Biodegradation of volatile organic compounds from paint industries,” *Appl. Biochem. Biotechnol.*, vol. 167, no. 3, pp. 564–580, Jun. 2012, doi: 10.1007/s12010-012-9706-8.

[48] S. Almaie, V. Vatanpour, M. H. Rasoulifard, and I. Koyuncu, “Volatile organic compounds (VOCs) removal by photocatalysts: A review,” Nov. 01, 2022, *Elsevier Ltd*. doi: 10.1016/j.chemosphere.2022.135655.

[49] W. C. Chung, D. H. Mei, X. Tu, and M. B. Chang, “Removal of VOCs from gas streams via plasma and catalysis,” Apr. 03, 2019, *Taylor and Francis Inc.* doi: 10.1080/01614940.2018.1541814.

[50] J. Geldermann, M. Treitz, H. Schollenberger, and O. Rentz, “Evaluation of VOC recovery strategies: Multi Objective Pinch Analysis (MOPA) for the evaluation of VOC recovery strategies,” *OR Spectrum*, vol. 28, no. 1, pp. 3–20, Jan. 2006, doi: 10.1007/s00291-005-0006-3.

[51] M. S. Kamal, S. A. Razzak, and M. M. Hossain, “Catalytic oxidation of volatile organic compounds (VOCs) - A review,” Sep. 01, 2016, *Elsevier Ltd*. doi: 10.1016/j.atmosenv.2016.05.031.

[52] R. Liu *et al.*, “Recent progress on catalysts for catalytic oxidation of volatile organic compounds: a review,” *Catal. Sci. Technol.*, vol. 12, no. 23, pp. 6945–6991, 2022, doi: 10.1039/D2CY01181F.

[53] Z. Zhang, Z. Jiang, and W. Shangguan, “Low-temperature catalysis for VOCs removal in technology and application: A state-of-the-art review,” *Catal. Today*, vol. 264, pp. 270–278, Apr. 2016, doi: 10.1016/j.cattod.2015.10.040.

[54] L. F. Liotta, “Catalytic oxidation of volatile organic compounds on supported noble metals,” Oct. 20, 2010. doi: 10.1016/j.apcatb.2010.08.023.

[55] C. J. Rhodes, “Properties and applications of zeolites,” *Sci. Prog.*, vol. 93, no. 3, pp. 223–284, Aug. 2010, doi: 10.3184/003685010X12800828155007.

[56] V. L. Zholobenko, A. Y. Khodakov, M. Impéror-Clerc, D. Durand, and I. Grillo, “Initial stages of SBA-15 synthesis: An overview,” Oct. 01, 2008. doi: 10.1016/j.cis.2008.05.003.

[57] L. Laskowski *et al.*, “New Class of Antimicrobial Agents: SBA-15 Silica Containing Anchored Copper Ions,” *J. Nanomater.*, vol. 2017, 2017, doi: 10.1155/2017/1287698.

[58] T. Barakat *et al.*, “Noble-metal-based catalysts supported on zeolites and macro-mesoporous metal oxide supports for the total oxidation of volatile organic compounds,” *ChemSusChem*, vol. 4, no. 10, pp. 1420–1430, Oct. 2011, doi: 10.1002/cssc.201100282.

[59] J. Weitkamp, “Zeolites and catalysis,” 2000. [Online]. Available: www.elsevier.com/locate/ssi

[60] S. Scirè, P. M. Riccobene, and C. Crisafulli, “Ceria supported group IB metal catalysts for the combustion of volatile organic compounds and the preferential oxidation of CO,” *Appl. Catal. B*, vol. 101, no. 1–2, pp. 109–117, Nov. 2010, doi: 10.1016/j.apcatb.2010.09.013.

[61] S. Gangopadhyay, D. D. Frolov, A. E. Masunov, and S. Seal, “Structure and properties of cerium oxides in bulk and nanoparticulate forms,” 2014, *Elsevier Ltd*. doi: 10.1016/j.jallcom.2013.09.013.

[62] S. Anirban, T. Paul, and A. Dutta, “Vacancy mediated ionic conduction in Dy substituted nanoceria: a structure-property correlation study,” *RSC Adv.*, vol. 5, no. 62, pp. 50186–50195, 2015, doi: 10.1039/c5ra06730h.

[63] H. S. Kim *et al.*, “Noble-Metal-Based Catalytic Oxidation Technology Trends for Volatile Organic Compound (VOC) Removal,” *Catalysts*, vol. 12, no. 1, Jan. 2022, doi: 10.3390/catal12010063.

[64] A. I. Stadnichenko, E. M. Slavinskaya, O. A. Stonkus, and A. I. Boronin, “Low-Temperature CO Oxidation by the Pt/CeO2 Based Catalysts,” Aug. 12, 2024, *John Wiley and Sons Inc*. doi: 10.1002/cctc.202301727.

[65] B. Bohigues *et al.*, “Overcoming activity/stability tradeoffs in CO oxidation catalysis by Pt/CeO2,” *Nature Communications* , vol. 16, no. 1, Dec. 2025, doi: 10.1038/s41467-025-62726-6.

[66] H. A. E. Dole and E. A. Baranova, “Ethylene Oxidation in an Oxygen-Deficient Environment: Why Ceria is an Active Support?,” *ChemCatChem*, vol. 8, no. 11, pp. 1977–1986, Jun. 2016, doi: 10.1002/cctc.201600142.

[67] M. B. Mooiman, K. C. Sole, and N. Dinham, “The Precious Metals Industry,” in *Metal Sustainability*, 2016, pp. 361–396. doi: https://doi.org/10.1002/9781119009115.ch16.

[68] J. A. Batten, C. Ciner, and B. M. Lucey, “The macroeconomic determinants of volatility in precious metals markets,” *Resources Policy*, vol. 35, no. 2, pp. 65–71, Jun. 2010, doi: 10.1016/j.resourpol.2009.12.002.

[69] I. Rumyk, V. Kuzminsky, O. Pylypenko, and O. Yaroshenko, “PRECIOUS METALS MARKET FORECASTING IN THE CURRENT ENVIRONMENT,” *Finance and Management Review*, vol. 1, no. 17, 2024, doi: 10.36690/2674.

[70] Z. Zhang, Z. Jiang, and W. Shangguan, “Low-temperature catalysis for VOCs removal in technology and application: A state-of-the-art review,” *Catal. Today*, vol. 264, pp. 270–278, Apr. 2016, doi: 10.1016/j.cattod.2015.10.040.

[71] K. Karpińska-Wlizło, W. Zawadzki, G. Słowik, and W. Gac, “Does the active surface area determine the activity of silica supported nickel catalysts in CO2 methanation reaction?,” *Chemical Engineering Journal*, vol. 502, Dec. 2024, doi: 10.1016/j.cej.2024.157827.

[72] G. Leofanti, M. Padovan, G. Tozzola, and B. Venturelli, “Surface area and pore texture of catalysts,” *Catal. Today*, 1998.

[73] C. Chen *et al.*, “Importance of platinum particle size for complete oxidation of toluene over Pt/ZSM-5 catalysts,” *Chemical Communications*, vol. 51, no. 27, pp. 5936–5938, Apr. 2015, doi: 10.1039/c4cc09383f.

[74] G. Boskovic and M. Baerns, “Catalyst Deactivation,” in *Basic Principles in Applied Catalysis*, M. Baerns, Ed., Berlin, Heidelberg: Springer Berlin Heidelberg, 2004, pp. 477–503. doi: 10.1007/978-3-662-05981-4_14.

[75] P. Forzatti and L. Lietti, “Catalyst deactivation,” *Catal. Today*, 1999.

[76] T. Andana *et al.*, “Ceria-supported small Pt and Pt3Sn nanoparticles for NOx-assisted soot oxidation,” *Appl. Catal. B*, vol. 209, pp. 295–310, 2017, doi: 10.1016/j.apcatb.2017.03.010.

[77] M. Piumetti, S. Bensaid, N. Russo, and D. Fino, “Nanostructured ceria-based catalysts for soot combustion: Investigations on the surface sensitivity,” *Appl. Catal. B*, vol. 165, pp. 742–751, Apr. 2015, doi: 10.1016/j.apcatb.2014.10.062.

[78] Q. Sun, X. Hu, S. Zheng, Z. Sun, S. Liu, and H. Li, “Influence of calcination temperature on the structural, adsorption and photocatalytic properties of TiO2 nanoparticles supported on natural zeolite,” *Powder Technol.*, vol. 274, pp. 88–97, Apr. 2015, doi: 10.1016/j.powtec.2014.12.052.

[79] S. Ballauri *et al.*, “Mesoporous Ceria and Ceria-Praseodymia as High Surface Area Supports for Pd-based Catalysts with Enhanced Methane Oxidation Activity,” *ChemCatChem*, vol. 16, no. 7, Apr. 2024, doi: 10.1002/cctc.202301359.

[80] Y. Wang, J. Ren, K. Deng, L. Gui, and Y. Tang, “Preparation of tractable platinum, rhodium, and ruthenium nanoclusters with small particle size in organic media,” *Chemistry of Materials*, vol. 12, no. 6, pp. 1622–1627, Jun. 2000, doi: 10.1021/cm0000853.

[81] I. A. Safo, M. Werheid, C. Dosche, and M. Oezaslan, “The role of polyvinylpyrrolidone (PVP) as a capping and structure-directing agent in the formation of Pt nanocubes,” *Nanoscale Adv.*, vol. 1, no. 8, pp. 3095–3106, 2019, doi: 10.1039/c9na00186g.

[82] P. Vyawahare, H. Tun, M. W. Vaughn, and C. C. Chen, “From Langmuir isotherm to Brunauer–Emmett–Teller isotherm,” *AIChE Journal*, vol. 68, no. 3, Mar. 2022, doi: 10.1002/aic.17523.

[83] R. B. Anderson, V. 68, and R. B. Anderson2, “Brunauer, Emmet and Teller Equation,” UTC, 1938. [Online]. Available: https://pubs.acs.org/sharingguidelines

[84] A. K. Singh, “Experimental Methodologies for the Characterization of Nanoparticles,” *Engineered Nanoparticles*, pp. 125–170, 2016, doi: 10.1016/b978-0-12-801406-6.00004-2.

[85] W. Zhou, Y. H. Ikuhara, Z. Zheng, K. Wang, B. Cao, and J. Chen, “Transmission electron microscopy (TEM) studies of functional nanomaterials,” *Modeling, Characterization, and Production of Nanomaterials: Electronics, Photonics, and Energy Applications, Second Edition*, pp. 467–512, Jan. 2023, doi: 10.1016/B978-0-12-819905-3.00017-8.

[86] C. Y. Tang and Z. Yang, “Transmission Electron Microscopy (TEM),” in *Membrane Characterization*, Elsevier Inc., 2017, pp. 145–159. doi: 10.1016/B978-0-444-63776-5.00008-5.

[87] A. A. Bunaciu, E. gabriela Udriştioiu, and H. Y. Aboul-Enein, “X-Ray Diffraction: Instrumentation and Applications,” Oct. 02, 2015, *Taylor and Francis Ltd.* doi: 10.1080/10408347.2014.949616.

[88] A. Bijelic and A. Rompel, “Polyoxometalates: more than a phasing tool in protein crystallography,” *ChemTexts*, vol. 4, no. 3, Oct. 2018, doi: 10.1007/s40828-018-0064-1.

[89] J. B. Nelson and D. P. Riley, “An experimental investigation of extrapolation methods in the derivation of accurate unit-cell dimensions of crystals,” *Proceedings of the Physical Society*, vol. 57, no. 3, p. 160, 1945, doi: 10.1088/0959-5309/57/3/302.

[90] D. A. M. Monti and A. Baiker, “Temperature-programmed reduction. Parametric sensitivity and estimation of kinetic parameters,” *J. Catal.*, vol. 83, no. 2, pp. 323–335, Oct. 1983, doi: 10.1016/0021-9517(83)90058-1.

[91] N. W. Hurst, S. J. Gentry, A. Jones, and B. D. McNicol, “Temperature Programmed Reduction,” *Catalysis Reviews*, vol. 24, no. 2, pp. 233–309, Jan. 1982, doi: 10.1080/03602458208079654.

[92] S. Marino, R. Taha, Y. Gu, W. Li, and W. Epling, “Adapted CO chemisorption technique to measure metal particle dispersion on ceria-containing catalysts,” 2024. [Online]. Available: https://www.elsevier.com/open-access/userlicense/1.0/

[93] B. E. Hayden, K. Kretzschmar, A. M. Bradshaw, and R. G. Greenler, “An infrared study of the adsorption of CO on a stepped platinum surface,” *Surf. Sci.*, vol. 149, no. 2–3, pp. 394–406, Jan. 1985, doi: 10.1016/0039-6028(85)90071-8.

[94] H. Steininger, S. Lehwald, and H. Ibach, “On the adsorption of CO on Pt(111),” *Surf. Sci.*, vol. 123, no. 2–3, pp. 264–282, Dec. 1982, doi: 10.1016/0039-6028(82)90328-4.

[95] S. Komai, Y. Yazawa, A. Satsuma, and T. Hattori, “Determination of Metal Dispersion of Pt/CeO2 Catalyst by CO-pulse Method,” *Journal of the Japan Petroleum Institute*, vol. 48, no. 3, pp. 173–177, 2005, doi: 10.1627/jpi.48.173.

[96] R. Peng *et al.*, “Size effect of Pt nanoparticles on the catalytic oxidation of toluene over Pt/CeO2 catalysts,” *Appl. Catal. B*, vol. 220, pp. 462–470, 2018, doi: 10.1016/j.apcatb.2017.07.048.

[97] J. C. Martínez-Munuera, M. P. Yeste, and A. García-García, “CO oxidation under lean and stoichiometric conditions over ceria-zirconia with very low metal contents (Cu, Co, Ag and Pt),” *Journal of Rare Earths*, vol. 42, no. 9, pp. 1669–1681, Sep. 2024, doi: 10.1016/j.jre.2023.08.015.

[98] T. Bligaard *et al.*, “Toward Benchmarking in Catalysis Science: Best Practices, Challenges, and Opportunities,” Apr. 01, 2016, *American Chemical Society*. doi: 10.1021/acscatal.6b00183.

[99] Y. F. Chen, C. Y. Lee, M. Y. Yeng, and H. T. Chiu, “The effect of calcination temperature on the crystallinity of TiO2 nanopowders,” *J. Cryst. Growth*, vol. 247, no. 3–4, pp. 363–370, Jan. 2003, doi: 10.1016/S0022-0248(02)01938-3.

[100] W. Kang, D. O. Ozgur, and A. Varma, “Solution Combustion Synthesis of High Surface Area CeO2 Nanopowders for Catalytic Applications: Reaction

Mechanism and Properties," *ACS Appl. Nano Mater.*, vol. 1, no. 2, pp. 675–685, Feb. 2018, doi: 10.1021/acsanm.7b00154.

[101] M. A. Al-Ghouti and D. A. Da'ana, "Guidelines for the use and interpretation of adsorption isotherm models: A review," *J. Hazard. Mater.*, vol. 393, p. 122383, Jul. 2020, doi: 10.1016/j.jhazmat.2020.122383.

[102] P. Shanmugam, G. Kuppuswamy, K. Pushparaj, B. Arumugam, A. Sundaramurthy, and Y. Sivalingam, "CeO2 Nanoparticles based Extended Gate Field Effect Transistor for Enzyme Free Detection of Glucose," *Journal of Materials Science: Materials in Electronics*, Apr. 2022, doi: 10.1007/s10854-021-07441-w.

[103] R. Jiang and C. Rong, "Ultrasound-assisted Micro-emulsion Synthesis of a Highly Active Nano-particle Catalyst," 2010.

[104] F. Zhang *et al.*, "Cerium oxide nanoparticles: Size-selective formation and structure analysis," *Appl. Phys. Lett.*, vol. 80, no. 1, pp. 127–129, Jan. 2002, doi: 10.1063/1.1430502.

[105] B. M. Reddy and A. Khan, "Nanosized CeO2-SiO2, CeO2-TiO2, and CeO2-ZrO2 mixed oxides: Influence of supporting oxide on thermal stability and oxygen storage properties of ceria," *Catalysis Surveys from Asia*, vol. 9, no. 3, pp. 155–171, Sep. 2005, doi: 10.1007/s10563-005-7552-1.

[106] A. I. Boronin *et al.*, "CO oxidation activity of Pt/CeO2 catalysts below 0 °C: platinum loading effects," *Appl. Catal. B*, vol. 286, no. 11, p. 119931, Jun. 2021, doi: 10.1016/j.apcatb.2021.119931.

[107] E. A. Lashina, E. M. Slavinskaya, O. A. Stonkus, and A. I. Boronin, "Abnormally narrow peaks in TPR-H2 over Pt/CeO2: Experiment and mathematical modelling," *Int. J. Hydrogen Energy*, vol. 89, pp. 590–604, Nov. 2024, doi: 10.1016/j.ijhydene.2024.09.253.

[108] O. Bunjaku *et al.*, "Understanding the Reducibility of CeO2 Surfaces by Proton–Electron Transfer from CpCr(CO)3H," *Inorg. Chem.*, vol. 63, no. 16, pp. 7512–7519, Apr. 2024, doi: 10.1021/acs.inorgchem.4c01199.

[109] L. F. Liotta, G. Di Carlo, F. Puleo, G. Pantaleo, and G. Deganello, "Mesoporous SBA-15 silica modified with cerium modification," 2010.

[110] M. Swanson, V. V. Pushkarev, V. I. Kovalchuk, and J. L. D'itri, "The dynamic surface chemistry during the interaction of CO with ceria captured by Raman spectroscopy," *Catal. Letters*, vol. 116, no. 1–2, pp. 41–45, Jul. 2007, doi: 10.1007/s10562-007-9087-8.

[111] E. R. Savinova and A. G. Oshchepkov, "Benchmarking in electrocatalysis," *Comprehensive Inorganic Chemistry III, Third Edition*, vol. 1–10, pp. 492–550, Jan. 2023, doi: 10.1016/B978-0-12-823144-9.00093-5.

[112] H. Wei *et al.*, "Morphological effect of ceria-supported platinum catalyst on low-temperature ethylene oxidation," *Appl. Catal. B*, vol. 324, May 2023, doi: 10.1016/j.apcatb.2022.122242.

[113] J. L. Vincent and P. A. Crozier, “Atomic level fluxional behavior and activity of CeO2-supported Pt catalysts for CO oxidation,” *Nat. Commun.*, vol. 12, no. 1, Dec. 2021, doi: 10.1038/s41467-021-26047-8.

[114] N. Bosio and H. Grönbeck, “Low Temperature CO Oxidation Over Pt/ceo2,” Sweden, 2021. [Online]. Available: https://www.proquest.com/dissertations-theses/low-temperature-co-oxidation-over-pt-ceo-sub-2/docview/2723855900/se-2?accountid=28840